



Available online at www.sciencedirect.com

ScienceDirect

Geochimica et Cosmochimica Acta 204 (2017) 179–204

**Geochimica et
Cosmochimica
Acta**

www.elsevier.com/locate/gca

Copper–arsenic decoupling in an active geothermal system: A link between pyrite and fluid composition

Daniele Tardani ^{a,b,*}, Martin Reich ^{a,b}, Artur P. Deditius ^c, Stephen Chryssoulis ^d,
Pablo Sánchez-Alfaro ^{a,b}, Jackie Wrage ^{a,b}, Malcolm P. Roberts ^e

^a Department of Geology, FCFM, Universidad de Chile, Santiago 8370450, Chile

^b Andean Geothermal Center of Excellence (CEGA), FCFM, Universidad de Chile, Santiago 8370450, Chile

^c School of Engineering and Information Technology, Murdoch University, Western Australia 6150, Australia

^d Advanced Mineral Technology Laboratory (AMTEL), London, Ontario N6G 4X8, Canada

^e Center for Microscopy, Characterisation and Analysis (CMCA), University of Western Australia, Crawley 6009, WA, Australia

Received 30 June 2016; accepted in revised form 25 January 2017; available online 3 February 2017

Abstract

Over the past few decades several studies have reported that pyrite hosts appreciable amounts of trace elements which commonly occur forming complex zoning patterns within a single mineral grain. These chemical zonations in pyrite have been recognized in a variety of hydrothermal ore deposit types (e.g., porphyry Cu–Mo–Au, epithermal Au deposits, iron oxide–copper–gold, Carlin-type and Archean lode Au deposits, among others), showing, in some cases, marked oscillatory alternation of metals and metalloids in pyrite growth zones (e.g., of Cu-rich, As–(Au, Ag)-depleted zones and As–(Au, Ag)-rich, Cu-depleted zones). This decoupled geochemical behavior of Cu and As has been interpreted as a result of chemical changes in ore-forming fluids, although direct evidence connecting fluctuations in hydrothermal fluid composition with metal partitioning into pyrite growth zones is still lacking. In this study, we report a comprehensive trace element database of pyrite from the Tolhuaca Geothermal System (TGS) in southern Chile, a young and active hydrothermal system where fewer pyrite growth rims and mineralization events are present and the reservoir fluid (i.e. ore-forming fluid) is accessible. We combined the high-spatial resolution and X-ray mapping capabilities of electron microprobe analysis (EMPA) with low detection limits and depth-profiling capacity of secondary-ion mass spectrometry (SIMS) in a suite of pyrite samples retrieved from a ~1 km drill hole that crosses the argillic (20–450 m) and propylitic (650–1000 m) alteration zones of the geothermal system. We show that the concentrations of precious metals (e.g., Au, Ag), metalloids (e.g., As, Sb, Se, Te), and base and heavy metals (e.g., Cu, Co, Ni, Pb) in pyrite at the TGS are significant. Among the elements analyzed, As and Cu are the most abundant with concentrations that vary from sub-ppm levels to a few wt.% (i.e., up to ~5 wt.% As, ~1.5 wt.% Cu). Detailed wavelength-dispersive spectrometry (WDS) X-ray maps and SIMS depth vs. isotope concentration profiles reveal that pyrites from the TGS are characterized by chemical zoning where the studied elements occur in different mineralogical forms. Arsenic and Co occur as structurally bound elements in pyrite, Cu and Au in pyrite can occur as both solid solution and submicron-sized particles of chalcopyrite and native Au (or Au tellurides), respectively. Pyrites from the deeper propylitic zone do not show significant zonation and high Cu–(Co)–As concentrations correlate with each other. In contrast, well-developed zonations were detected in pyrite from the shallow argillic alteration zone, where Cu(Co)-rich, As-depleted cores alternate with Cu(Co)-depleted, As-rich rims. These microanalytical data were contrasted with chemical data of fluid inclusions in quartz and calcite veins (high Cu/As ratios) and borehole fluid (low Cu/As ratios) reported at the TGS, showing a clear correspondence between Cu and As concentrations in pyrite-forming fluids and chemical zonation in pyrite. These observations provide direct evidence supporting the selective partitioning of metals into pyrite as a result of changes in ore-forming fluid

* Corresponding author at: Department of Geology, FCFM, Universidad de Chile, Santiago 8370450, Chile.
E-mail address: daniele.tardani@ing.uchile.cl (D. Tardani).

composition, most likely due to separation of a single-phase fluid into a low-density vapor and a denser brine, capable of fractionating Cu and As.

© 2017 Elsevier Ltd. All rights reserved.

Keywords: Trace elements; Pyrite; Cu–As decoupling; Tolhuaca Geothermal System; Southern Volcanic Zone

1. INTRODUCTION

Sulfide minerals are common in many active geothermal systems worldwide, including the Salton Sea in California (Skinner et al., 1967; McKibben and Elders, 1985; McKibben et al., 1988a,b; Hulen et al., 2004), Rotokawa, Ngawha and Broadlands-Ohaaki in New Zealand (Krupp and Seward, 1987; Cox and Browne, 1995; Simmons and Browne, 2000), Kirishima and Yanaizu-Nishiyama in Japan (Shoji et al., 1989, 1999), Mataloko in Indonesia (Koseki and Kazuo, 2006; Koseki and Nakashima, 2006), Joaquina in Guatemala (Libbey et al., 2015) and Reykjanes in Iceland (Libbey and Williams-Jones, 2016). Among sulfides, pyrite is ubiquitous in geothermal systems although most studies have focused on their metal-rich fossil counterparts (i.e., ore deposits). Mineral chemistry studies of pyrite in hydrothermal ore deposits, including Carlin-type and Archean lode Au deposits, porphyry Cu deposits, epithermal Au–Ag deposits and iron oxide–copper–gold deposits (IOCG), among others, have pointed out that this sulfide is a major host of metals and metalloids such as Au, Ag, Cu, Pb, Zn, Co, Ni, As, Sb, Se, Te, Hg, Tl, and Bi (Cook and Chryssoulis, 1990; Fleet et al., 1993; Huston et al., 1995; Simon et al., 1999; Palenik et al., 2004; Vaughan and Kyin, 2004; Reich et al., 2005, 2006; Large et al., 2009; Barker et al., 2009; Cook et al., 2009; Deditius et al., 2009a,b, 2011, 2014; Sung et al., 2009; Koglin et al., 2010; Ulrich et al., 2011; Peterson and Mavrogenes, 2014; Steadman et al., 2015; Gregory et al., 2016; Reich et al., 2016, 2017; Tanner et al., 2016). These studies have also provided analytical and spectroscopic evidence showing that the incorporation and micro-textural distribution of these elements is complex in pyrite, occurring in both solid solution and/or as metal nanoparticles or nano-inclusions forming chemically-heterogeneous growth and sector zones. This variation in the chemical composition of pyrite has been used to elucidate the chemical evolution of hydrothermal systems and ore deposits at various scales (Muntean et al., 2011), and has also been evaluated as a vectoring tool in mineral exploration (Baker et al., 2006; Belousov et al., 2014; Franchini et al., 2015; Gregory et al., 2016; Soltani et al., 2015). More recently, trace element contents in marine sulfides, particularly pyrite, are being used to answer some fundamental questions about the evolution of the Earth's ocean–atmosphere system, including how nutrient trace element cycles relate to geodynamic cycles, biological evolution and mass extinction events (Large et al., 2014, 2015a,b; Gregory et al., 2015a, b; Long et al., 2015).

Recent studies have reported complex oscillatory growth and sector zoning in pyrite from hydrothermal ore deposits where elements such Cu, Au and As are preferentially

enriched and show a decoupled geochemical behavior (Deditius et al., 2008, 2009a,b, 2011; Reich et al., 2013). Arsenic-rich zones containing Au, Ag, Sb, Te, and Pb, can alternate with Cu-rich zones with significantly lower concentrations of these elements, and barren pyrite zones with no other elements. These chemical zoning features have been related to selective partitioning of metals into pyrite as the result of physico-chemical changes in the ore-forming fluids (Deditius et al., 2009a,b; Reich et al., 2013, 2016, 2017; Peterson and Mavrogenes, 2014). Furthermore, in low-temperature sedimentary environments, recent studies have shown that diagenetic pyrite formed within the anoxic sediments can record the composition of pore water (Berner et al., 2006, 2013; Gregory et al., 2014).

In particular, the presence of finely spaced multiple growth zones in pyrite where Cu and As are geochemically decoupled provide evidence that the composition of shallow hydrothermal systems can be affected intermittently and repetitively by vapors, probably from underlying magmas (Deditius et al., 2009a,b; Reich et al., 2013). However, direct observations linking the alternating metal concentrations in pyrite zonations and the chemical evolution of the ore-forming fluid are still lacking. Furthermore, in active geothermal systems very few studies report trace metal concentrations in pyrite (e.g. Reykjanes geothermal system; Libbey and Williams-Jones, 2016), and no data linking sulfide composition, paleofluid and present-day fluid chemistry are currently available. Such information is relevant and is feasible to obtain in a young, active geothermal system where fewer mineralization events are present, pyrite show fewer growth zones and/or chemical oscillations, and the reservoir fluid (i.e. ore-forming fluid) is accessible. This evidence is crucial to interpret the reportedly complex zoning of pyrite in fossil hydrothermal systems.

In this paper we report a comprehensive major and trace element database of pyrite from the active Tolhuaca Geothermal System (TGS) in the Andes of southern Chile, a high enthalpy geothermal reservoir that has been drilled down to ~2 km depth, but has not been affected by geothermal production or re-injection (Melosh et al., 2012; Sánchez-Alfaro et al., 2016a). At the TGS fine-grained pyrite is abundant, the present-day well fluid carry metals and metalloids including Cu, Au and As, among others, and paleofluids compositions are also available from fluid inclusions studies (Sánchez-Alfaro et al., 2016a). Therefore, the TGS provides an excellent opportunity to link the chemical and textural features of pyrite with paleofluids and bore-hole fluid composition data. In situ concentrations of precious metals (e.g., Au, Ag), metalloids (e.g., As, Sb, Se, Te) and base and heavy metals (e.g., Cu, Co, Ni, Pb) were measured using a combination of electron microprobe analysis (EMPA) and secondary-ion mass spectrometry

(SIMS) in a suite of well constrained pyrite samples retrieved from a ~1 km drill core. Furthermore, we correlated our pyrite trace element data with geochemical data of present-day borehole fluid samples and LA-ICP-MS analyses of fluid inclusion assemblages hosted in paragenetically-linked quartz and calcite veins from Sánchez-Alfaro et al. (2016a). By integrating these three sources of data, i.e., elemental concentrations in pyrite, fluid inclusions data and borehole fluid chemistry, we provide evidence that fluctuations in the trace element budget of pyrite are directly linked to changes in hydrothermal fluid composition resulting from episodic inputs of magmatic vapor and/or phase separation (or boiling) of a single-phase hydrothermal fluid.

2. GEOLOGICAL BACKGROUND

In the Andean Cordillera of the central-southern Chile, hydrothermal systems occur in close spatial relationships with active volcanism as well as with major seismically active fault systems (Cembrano and Lara, 2009). In this region, geothermal features are spatially related with the Liquiñe-Ofqui Fault System and with the NW-trending Arc-oblique Long-lived Basement Fault System (Sánchez et al., 2013; Tardani et al., 2016). The active TGS is located in the northern termination of the Liquiñe-Ofqui Fault System (Fig. 1) and is spatially associated with both NE- and NW-striking faults.

The Tolhuaca volcano is a glacially scoured composite stratovolcano of late-Pleistocene to Holocene age that rises ~900 m over a Miocene volcano-sedimentary rock basement (Thiele et al., 1987; Lohmar et al., 2012). In the summit, several NW-trending aligned craters with different preservation states indicate a migration of the volcanic activity from the SE towards the NW (Thiele et al., 1987). Lavas are predominantly basaltic andesites and andesites, with minor presence of basalts and dacites (Thiele et al., 1987; Lohmar et al., 2012). The latest eruptive phases occur in the NW portion of the volcanic edifice and correspond to a ~2 km long NW-trending fissure and a pyroclastic cone. The Tolhuaca volcano is likely to be related to the ALFS, which provides the suitable conditions for the development of magma reservoirs and magma differentiation (Cembrano and Lara, 2009; Pérez-Flores et al., 2016).

The TGS is located in the northwest flank of the Tolhuaca volcano and is characterized by several surficial thermal manifestations including fumaroles, boiling pools and hot springs (Fig. 1). Geothermal exploration campaigns have revealed the existence of a high-enthalpy reservoir in the system (Melosh et al., 2010, 2012). Two slim holes (Tol-1 and Tol-2) and two larger diameter wells (Tol-3 and Tol-4) were drilled down to 2117 m vertical depth (Fig. 1). Temperature logging and fluid samples suggest the presence of a geothermal reservoir at c.a. 1.5 km depth, at liquid-saturated conditions with temperatures up to 300 °C and a relatively high meteoric water component (Melosh et al., 2012). The main reservoir is overlain by a steam heated aquifer at shallow depths that reaches up to 160 °C and controls the chemical nature of most of the hot springs (Melosh et al., 2010, 2012).

The different geologic units, observed in the Tol-1 drill core material, are mainly lavas and related breccias, volcanoclastics and minor tuffs (Fig. 1). Hyaloclastites and pillow breccias also occur at different levels in the Tol-1 core (Lohmar et al., 2012; Sánchez-Alfaro et al., 2016a). Based on thin section petrography and X-ray diffraction (XRD) analyses of the Tol-1 core, three alteration zones were defined: (1) an upper zone of argillic alteration (20–450 m); (2) an intermediate zone with sub-propylitic alteration (450–650 m); and (3) a deeper zone of propylitic alteration (\geq 650 m) (Fig. 1) (Melosh et al., 2012). Lohmar et al. (2012) and Sánchez-Alfaro et al. (2016a) characterized argillic alteration facies by Fe-oxides + chlorite + calcite + clay + quartz + pyrite (+apatite), whereas the mineral assemblages in high temperature propylitic facies are composed of chlorite + epidote + calcite + pyrite + quartz + zeolites.

Melosh et al. (2012) and Sánchez-Alfaro et al. (2016a) recognized four stages (S1 to S4) of hydrothermal alteration in the TGS. The S1 stage represents an early heating event characterized by precipitation of iron oxides, quartz, and chalcedony as a result of widespread boiling and flushing. An episode of pervasive hydrothermal alteration of the volcanic and volcaniclastic rocks defines the S2 stage, where low temperature (<200 °C) argillic alteration assemblages (smectite; illite/smectite; interlayered chlorite/smectite, pyrite, calcite and chalcedony/amorphous silica) developed at the shallower levels (<670 m), while propylitic alteration assemblages (chlorite, epidote, quartz, calcite and pyrite) were formed under higher temperature (\geq 250 °C) conditions in the deep upflow zone (>700 m). Between the S2 and S3 stages, a low-permeability clay cap composed of chlorite and smectite was formed, separating the deep part of the system (propylitic alteration) from the shallower one (argillic alteration) (Fig. 1). The S3 stage was characterized by an increase in magmatic heat that promoted hydrofracturing and brecciation of the clay-cap. The homogenization temperature data from fluid inclusions indicate diffuse boiling in the upper and lower zones. Finally, the S4 stage reveals a phase of fluid mixing and gentle boiling.

3. SAMPLES AND METHODS

Six representative pyrite-bearing samples from the argillic and propylitic alteration zones were selected (PFI-2, PFI-3, PFI-26, PFI-39, PFI-41, and PFI-45) from different depths of the drill core, as shown in Fig. 1. Scanning electron microscope (SEM) observations were undertaken at the Andean Geothermal Centre of Excellence (CEGA), Universidad de Chile, using a FEI Quanta 250 SEM equipped with secondary electron (SE), energy-dispersive X-ray spectrometry (EDS), backscattered electron (BSE) and cathodoluminescence (CL) detectors. The analytical parameters were: spot size of 1–3 μm, an accelerating voltage of 10–20 keV, a beam intensity of 80 μA, and a working distance of 10 mm.

Pyrite is present as euhedral or sub-euhedral disseminated grains (<1 mm) at the TGS, occurring in millimeter-sized monomineralic veinlets and in micrometer-sized crystals in the rim of veins of amorphous

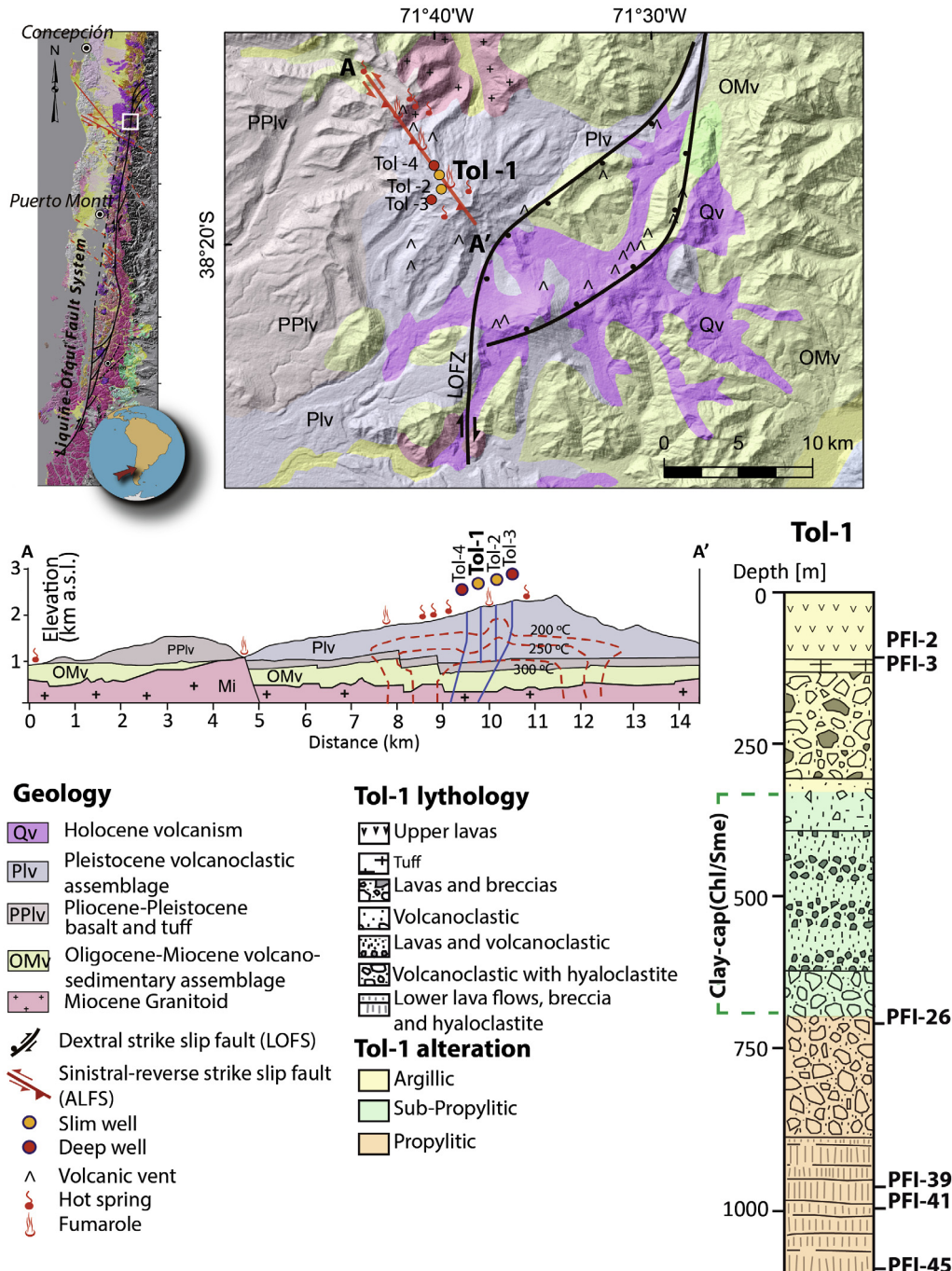


Fig. 1. Geological map of the Tolhuaca Geothermal System (TGS), modified from Aravena et al. (2016) and Sánchez-Alfaro et al. (2016a). The main geologic units, structures, surface thermal features and geothermal well locations, as well as the schematic cross section, were modified from Sánchez-Alfaro et al. (2016a). Simplified lithology of the Tol-1 well and hydrothermal alteration zones were taken from Melosh et al. (2010, 2012) and Sánchez et al. (2013). Depth location is indicated for pyrite-bearing samples PFI-2, PFI-3, PFI-26, PFI-39, PFI-41 and PFI-45. LOFZ: Liquiñe Ofqui Fault Zone; ALFS: Arc-oblique Long-lived Basement Fault System.

silica and Fe-oxides (Fig. 2). Pyrite is generally fine-grained in the deeper propylitic zone ($<30 \mu\text{m}$). In the sub-propylitic zone (clay cap), pyrite is almost absent and is replaced by minor chalcopyrite and bornite. Minor amounts of sphalerite and galena are also identified. For detailed descriptions of the alteration and mineralization

assemblages at Tolhuaca, the reader is referred to Sánchez-Alfaro et al. (2016a).

Electron microprobe analysis (EMPA) of pyrite grains (152 spot analyses total) was performed using a field-emission JEOL 8530F hyperprobe equipped with five wavelength-dispersive spectrometers at the Center for

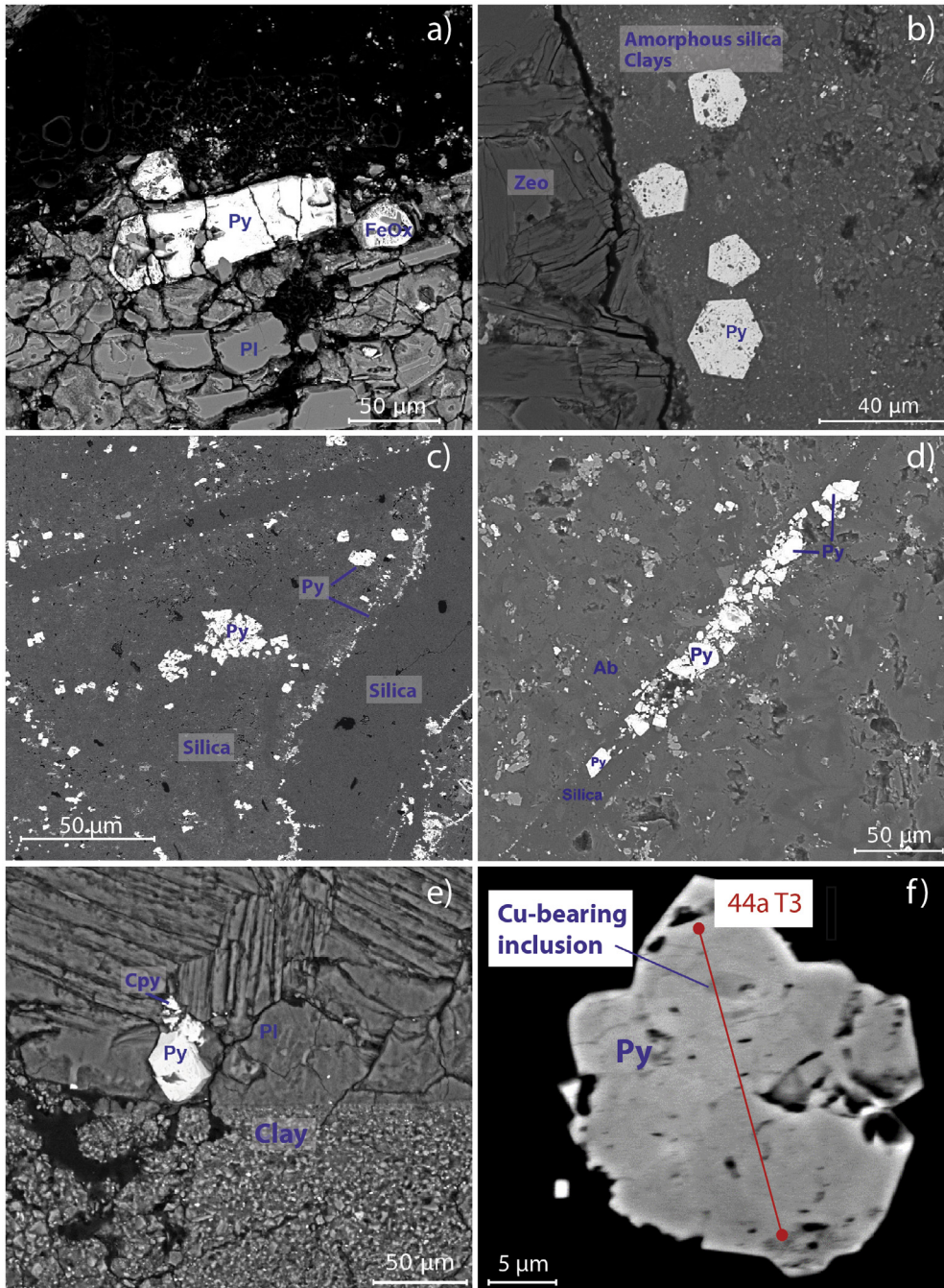


Fig. 2. Backscattered electron (BSE) images showing representative textural relationships of pyrite-bearing samples from the TGS. Pyrite occurs as disseminated grains (A, B, C, E, F) and in silica veinlets (C, D), and is mainly associated with Fe-oxide (A) and chalcopyrite (E). Chalcopyrite inclusions in pyrite are visible in selected grains (F). Py: pyrite; FeOx: Fe-oxide; Zeo: zeolite; Ab: albite, Cpy: chalcopyrite. The red line (F) shows an EMPA traverse (see Table 1, sample PFI-39, datapoints 44a T3).

Microscopy, Characterization and Analysis (CMCA), University of Western Australia in Crawley, WA. Operating conditions were 40 degrees take-off angle and beam energy of 20 keV. The beam current was 50 nA, and the beam was fully focused. Elements were acquired using the following analyzing crystals: LiF for Fe K α , Au L α , Te L α , Cu K α , Ni K α , Zn K α and Co K α ; PETJ for S K α ,

Ag L α , and Cd L α ; PETH for Sb L α , and Pb M α ; and TAP for As L α and Se L α . The standards employed were commercially available metals, oxides, sulfides, selenides, and tellurides. Counting time was 20 s for S K α and Fe K α , 60 s for Cu K α , Ni K α , Zn K α , and Co K α , 80 s for Se L α and Te L α , 100 s for As L α , Sb L α , and Pb M α , 120 s for Ag L α and Cd L α , and 200 s for Au L α . Mean

Table 1

Representative EPMA analyses (wt%) of pyrite from the Tolhuaca Geothermal System. Detection limits (DL) are shown in wt.%.

	S WT%	Fe WT%	Co WT%	Cu WT%	Ni WT%	Pb WT%	Ti WT%	As WT%	Sb WT%	Se WT%	Te WT%	Au WT%	Ag WT%	Cd WT%	TOTAL
DL	0.01	0.02	0.01	0.01	0.01	0.01	0.01	0.01	0.01	0.01	0.01	0.03	0.01	0.02	
<i>PFI-2</i>															
p1-1	50.83	45.07	0.01	0.03	b.d.	0.03	b.d.	2.72	0.01	b.d.	b.d.	b.d.	b.d.	b.d.	98.75
p1-2	51.67	44.70	0.01	b.d.	0.01	0.02	b.d.	3.93	0.02	0.01	b.d.	b.d.	b.d.	0.03	100.47
p3-1	52.18	44.42	0.11	0.02	0.04	0.11	b.d.	2.35	0.01	0.01	b.d.	b.d.	0.02	0.03	99.30
p2-1	51.37	44.62	b.d.	b.d.	b.d.	0.03	b.d.	2.95	0.01	b.d.	b.d.	b.d.	b.d.	b.d.	99.09
p5-1	53.16	44.51	0.10	0.33	0.02	0.24	b.d.	b.d.	0.01	b.d.	b.d.	b.d.	0.03	0.04	98.43
p4-1	53.16	44.88	0.02	0.47	b.d.	0.10	b.d.	0.30	b.d.	b.d.	b.d.	b.d.	0.02	b.d.	98.99
p8-1	53.09	45.01	0.10	0.09	0.01	0.17	b.d.	0.50	0.02	0.03	b.d.	b.d.	0.02	b.d.	99.13
p8-2	51.79	43.93	0.05	0.36	0.01	0.08	b.d.	0.43	b.d.	b.d.	b.d.	b.d.	0.02	0.02	96.70
p8-3	53.09	44.52	0.06	0.05	0.01	0.08	b.d.	0.15	b.d.	b.d.	b.d.	b.d.	0.02	0.02	98.02
p8-4	52.78	43.90	0.02	0.06	b.d.	0.04	b.d.	0.89	b.d.	b.d.	b.d.	b.d.	0.02	0.04	97.75
p7-1	50.01	45.23	0.11	0.03	0.06	0.06	b.d.	b.d.	0.01	b.d.	0.04	b.d.	b.d.	b.d.	95.60
p7-2	52.79	45.47	b.d.	0.14	b.d.	0.02	b.d.	b.d.	0.01	b.d.	0.05	b.d.	b.d.	b.d.	98.58
p7-3	53.54	45.17	0.01	0.03	b.d.	b.d.	b.d.	0.33	b.d.	b.d.	b.d.	b.d.	0.03	0.02	99.13
p6-1	50.17	43.53	0.04	0.33	b.d.	0.16	b.d.	4.88	0.03	0.04	0.04	b.d.	b.d.	b.d.	99.26
<i>PFI-3</i>															
p3-1	52.76	44.82	0.06	0.08	b.d.	0.15	b.d.	b.d.	0.01	0.01	b.d.	b.d.	b.d.	b.d.	97.92
p3-4	51.67	44.27	b.d.	0.24	b.d.	0.07	b.d.	b.d.	0.01	b.d.	b.d.	b.d.	0.02	96.31	
p4-1	52.15	44.94	0.24	0.06	0.03	0.07	b.d.	0.08	0.02	b.d.	b.d.	b.d.	0.02	b.d.	97.67
p4-2	52.07	44.88	0.06	0.08	b.d.	0.12	b.d.	b.d.	0.01	b.d.	b.d.	b.d.	0.02	97.29	
p4-3	51.46	44.55	0.04	0.11	b.d.	0.19	b.d.	b.d.	0.01	b.d.	b.d.	b.d.	0.02	b.d.	96.43
p4-4	51.74	45.04	0.05	0.03	b.d.	0.06	b.d.	b.d.	0.01	b.d.	b.d.	b.d.	b.d.	b.d.	96.98
p4-5	51.27	44.20	0.18	0.12	0.02	0.15	b.d.	b.d.	0.02	b.d.	b.d.	b.d.	0.02	b.d.	96.04
p1-2	51.60	44.95	0.18	0.09	0.02	0.07	b.d.	b.d.	0.01	b.d.	b.d.	b.d.	0.02	b.d.	96.97
p1-4	51.95	45.84	0.03	0.13	0.01	0.06	b.d.	0.19	0.01	b.d.	b.d.	b.d.	b.d.	b.d.	98.26
p1-5	51.16	45.46	0.01	0.03	b.d.	0.01	b.d.	0.86	0.02	b.d.	b.d.	b.d.	b.d.	b.d.	97.58
p2-4	51.29	45.59	0.04	0.06	b.d.	0.03	b.d.	0.07	0.02	b.d.	b.d.	b.d.	b.d.	b.d.	97.12
p2-5	52.03	45.74	0.03	0.08	b.d.	0.02	b.d.	0.06	0.01	b.d.	b.d.	b.d.	b.d.	b.d.	98.00
p2-7	51.08	44.78	0.10	0.04	b.d.	0.17	b.d.	b.d.	0.01	b.d.	b.d.	b.d.	b.d.	b.d.	96.20
p2-8	51.72	45.25	0.06	0.10	b.d.	0.04	b.d.	0.19	0.02	b.d.	b.d.	b.d.	b.d.	b.d.	97.43
p5-2	51.55	45.42	0.06	0.09	b.d.	0.08	b.d.	0.08	0.01	b.d.	0.05	b.d.	b.d.	b.d.	97.38
p5-5	51.79	44.66	0.07	0.08	b.d.	0.12	b.d.	b.d.	0.01	b.d.	b.d.	b.d.	0.02	b.d.	96.82
p7-1	50.01	44.39	0.05	0.07	b.d.	0.07	b.d.	0.53	0.02	0.01	b.d.	b.d.	b.d.	b.d.	95.17
p7-4	51.49	45.44	b.d.	0.20	b.d.	0.03	b.d.	0.11	0.02	b.d.	b.d.	b.d.	b.d.	b.d.	97.33
p7-5	51.93	45.06	0.03	0.07	b.d.	0.02	b.d.	0.29	0.02	b.d.	b.d.	b.d.	0.02	b.d.	97.47
<i>PFI-39</i>															
8a	53.76	45.45	0.03	b.d.	b.d.	b.d.	b.d.	b.d.	0.01	0.04	b.d.	b.d.	0.03	0.07	99.38
9a	52.54	45.95	0.03	b.d.	0.02	98.54									
10a	53.32	46.24	0.08	b.d.	b.d.	b.d.	b.d.	b.d.	0.16	b.d.	b.d.	b.d.	0.04	99.85	
12a	54.75	46.52	0.04	0.10	b.d.	b.d.	b.d.	b.d.	0.12	b.d.	b.d.	b.d.	0.03	0.05	101.62

19a	52.56	45.37	0.05	b.d.	b.d.	b.d.	b.d.	0.06	b.d.	b.d.	b.d.	b.d.	b.d.	0.04	98.08
24a	54.01	46.63	0.04	b.d.	b.d.	b.d.	b.d.	0.01	b.d.	b.d.	b.d.	b.d.	b.d.	0.04	100.72
26a	54.08	46.17	0.04	b.d.	b.d.	b.d.	b.d.	0.15	b.d.	b.d.	b.d.	b.d.	b.d.	0.02	100.49
29a	52.75	45.96	0.05	b.d.	b.d.	0.06	b.d.	1.77	0.02	b.d.	b.d.	b.d.	b.d.	0.02	100.65
30a	53.73	46.07	0.10	b.d.	b.d.	0.03	b.d.	0.18	b.d.	b.d.	b.d.	b.d.	b.d.	0.02	100.18
31a	54.37	46.80	0.07	b.d.	b.d.	0.02	b.d.	0.04	0.01	b.d.	b.d.	b.d.	b.d.	0.03	101.34
32a(T1)	53.25	46.93	0.06	b.d.	b.d.	0.01	b.d.	0.03	100.27						
32a(T1)	53.03	46.59	0.08	b.d.	b.d.	0.03	b.d.	0.22	b.d.	b.d.	b.d.	b.d.	b.d.	0.03	99.99
32a(T1)	53.73	46.79	0.07	b.d.	0.03	100.62									
32a(T1)	54.25	46.87	0.06	b.d.	b.d.	b.d.	b.d.	0.04	b.d.	b.d.	b.d.	b.d.	b.d.	0.03	101.25
32a(T1)	53.63	46.74	0.07	b.d.	b.d.	0.06	b.d.	0.66	0.01	b.d.	b.d.	b.d.	b.d.	0.04	101.20
32a(T1)	53.67	46.71	0.06	b.d.	b.d.	0.02	b.d.	0.05	b.d.	b.d.	b.d.	b.d.	b.d.	0.02	100.56
32a(T1)	53.40	46.61	0.07	b.d.	b.d.	0.04	b.d.	0.35	b.d.	b.d.	b.d.	b.d.	b.d.	0.04	100.50
33a	52.52	46.50	0.08	b.d.	b.d.	0.03	b.d.	0.13	b.d.	b.d.	b.d.	b.d.	b.d.	0.04	99.28
34a(T2)	53.18	46.25	0.11	b.d.	b.d.	0.05	b.d.	0.21	b.d.	b.d.	b.d.	b.d.	b.d.	0.02	99.88
34a(T2)	53.62	46.67	0.04	b.d.	0.04	100.36									
34a(T2)	53.56	46.75	0.04	b.d.	0.02	100.42									
34a(T2)	53.24	46.39	0.06	b.d.	b.d.	b.d.	b.d.	0.06	b.d.	b.d.	b.d.	b.d.	b.d.	0.02	99.81
36a	53.80	46.50	0.04	b.d.	b.d.	0.02	b.d.	0.25	0.01	b.d.	b.d.	b.d.	b.d.	0.04	100.67
39a	53.85	46.41	0.03	b.d.	0.05	100.34									
40a	53.80	46.17	0.04	0.01	b.d.	0.01	0.02	0.03	0.01	0.01	b.d.	b.d.	b.d.	0.03	100.18
41a	52.64	46.12	0.04	0.02	b.d.	b.d.	0.07	b.d.	b.d.	b.d.	b.d.	b.d.	b.d.	0.04	98.92
42a	53.56	46.15	0.03	b.d.	0.02	99.81									
44a(T3)	53.51	46.64	0.06	b.d.	0.04	100.25									
44a(T3)	53.00	45.89	0.07	1.58	b.d.	0.05	b.d.	b.d.	0.01	b.d.	b.d.	b.d.	b.d.	0.03	100.64
44a(T3)	53.72	46.87	0.07	0.06	b.d.	0.04	b.d.	0.02	100.81						
44a(T3)	52.95	46.64	0.08	b.d.	b.d.	0.03	b.d.	0.03	b.d.	b.d.	b.d.	b.d.	b.d.	0.02	99.74
44a(T3)	52.80	45.99	0.07	b.d.	b.d.	0.01	b.d.	0.03	98.91						
44a(T3)	53.25	46.34	0.05	b.d.	0.04	99.69									
45a(T4)	52.84	46.01	0.06	0.02	b.d.	0.02	b.d.	1.19	0.03	b.d.	b.d.	b.d.	b.d.	0.02	100.22
45a(T4)	51.77	44.93	0.05	0.05	b.d.	2.04	b.d.	1.17	0.02	b.d.	b.d.	b.d.	b.d.	0.04	100.07
45a(T4)	51.38	45.23	0.04	b.d.	b.d.	1.34	b.d.	1.32	0.02	b.d.	b.d.	b.d.	b.d.	b.d.	99.33
46a(T5)	53.95	46.40	0.05	b.d.	b.d.	b.d.	b.d.	0.39	b.d.	b.d.	b.d.	b.d.	b.d.	0.02	100.85
46a(T5)	53.98	46.51	0.04	b.d.	b.d.	b.d.	b.d.	0.36	b.d.	b.d.	b.d.	b.d.	b.d.	0.02	100.95
46a(T5)	53.83	46.81	0.04	b.d.	b.d.	b.d.	b.d.	0.26	0.01	b.d.	b.d.	b.d.	b.d.	0.02	101.01
46a(T5)	53.32	46.44	0.05	0.04	b.d.	0.02	b.d.	0.22	0.01	b.d.	b.d.	b.d.	b.d.	0.04	100.14
46a(T5)	53.79	46.97	0.11	b.d.	b.d.	0.02	b.d.	0.43	0.01	b.d.	b.d.	b.d.	b.d.	0.04	101.38
46a(T5)	53.33	46.66	0.07	b.d.	b.d.	0.02	b.d.	0.36	0.01	b.d.	b.d.	b.d.	b.d.	0.03	100.47
46a(T5)	53.48	46.75	0.07	b.d.	b.d.	b.d.	b.d.	0.26	0.01	b.d.	b.d.	b.d.	b.d.	0.03	100.60
47a	53.42	45.71	0.14	b.d.	b.d.	b.d.	b.d.	0.06	0.62	0.03	b.d.	b.d.	b.d.	0.02	100.04
49a	53.09	46.26	0.19	b.d.	b.d.	b.d.	b.d.	0.04	0.98	0.01	b.d.	b.d.	b.d.	0.03	100.60
50a	52.97	46.82	0.07	b.d.	b.d.	b.d.	b.d.	0.62	0.03	b.d.	b.d.	b.d.	b.d.	0.03	100.53

(continued on next page)

Table 1 (continued)

DL	S WT% 0.01	Fe WT% 0.02	Co WT% 0.01	Cu WT% 0.01	Ni WT% 0.01	Pb WT% 0.01	Ti WT% 0.01	As WT% 0.01	Sb WT% 0.01	Se WT% 0.01	Te WT% 0.01	Au WT% 0.03	Ag WT% 0.01	Cd WT% 0.02	TOTAL
<i>PFI-4I</i>															
1b(T1)	54.46	46.43	0.04	b.d.	0.04	0.04	101.02								
1b(T1)	54.16	46.69	0.04	b.d.	0.03	0.06	100.98								
1b(T1)	54.05	46.92	0.04	b.d.	0.04	101.04									
1b(T1)	53.72	46.75	0.04	b.d.	0.04	100.55									
1b(T1)	53.68	46.69	0.04	b.d.	b.d.	b.d.	b.d.	b.d.	0.01	b.d.	b.d.	b.d.	b.d.	0.03	100.44
1b(T1)	53.44	46.63	0.04	b.d.	b.d.	0.01	b.d.	0.03	100.15						
1b(T1)	53.43	46.72	0.05	b.d.	b.d.	0.01	b.d.	b.d.	0.01	b.d.	b.d.	b.d.	b.d.	0.02	100.24
2b	53.87	46.48	0.04	b.d.	b.d.	0.01	b.d.	0.04	100.45						
4b	54.09	46.77	0.05	b.d.	b.d.	0.02	b.d.	b.d.	b.d.	b.d.	b.d.	b.d.	0.02	0.04	100.99
5b	53.53	46.43	0.08	b.d.	b.d.	0.04	b.d.	0.03	100.11						
6b	53.51	46.42	0.03	b.d.	b.d.	0.01	b.d.	0.04	100.02						
7b	53.53	46.59	0.04	b.d.	b.d.	b.d.	b.d.	b.d.	0.01	b.d.	b.d.	b.d.	b.d.	0.03	100.20
8b	53.90	46.13	0.04	b.d.	b.d.	b.d.	b.d.	0.37	b.d.	b.d.	b.d.	b.d.	0.03	0.05	100.51
9b	54.08	46.56	0.04	b.d.	b.d.	b.d.	b.d.	0.12	b.d.	b.d.	b.d.	b.d.	0.03	0.04	100.87
10b	52.95	46.24	0.05	b.d.	b.d.	b.d.	b.d.	0.55	0.01	b.d.	b.d.	b.d.	b.d.	0.04	99.82
11b	53.07	46.24	0.08	b.d.	b.d.	0.04	0.15	b.d.	99.58						
12b	54.51	46.40	0.06	b.d.	b.d.	b.d.	0.08	0.16	0.01	b.d.	b.d.	b.d.	0.03	0.03	101.27
13b	52.68	45.70	0.04	b.d.	b.d.	b.d.	0.06	0.10	b.d.	b.d.	b.d.	b.d.	0.02	0.03	98.63
14b	53.62	46.71	0.06	b.d.	b.d.	0.02	0.12	b.d.	b.d.	b.d.	b.d.	b.d.	0.02	0.03	100.57
15b	53.61	46.47	0.05	b.d.	b.d.	0.02	0.07	0.13	b.d.	b.d.	b.d.	b.d.	b.d.	0.03	100.38
16b	53.69	46.26	0.11	b.d.	b.d.	0.02	0.13	b.d.	b.d.	b.d.	b.d.	b.d.	b.d.	0.03	100.24
17b	52.41	45.62	0.11	b.d.	b.d.	0.02	0.11	0.10	0.01	b.d.	b.d.	b.d.	b.d.	0.03	98.42
20b	53.40	46.28	0.05	b.d.	b.d.	0.04	0.04	b.d.	0.01	b.d.	b.d.	b.d.	b.d.	0.02	99.84
21b	53.25	45.92	0.04	b.d.	b.d.	0.02	0.06	0.22	0.01	b.d.	b.d.	b.d.	b.d.	0.02	99.57
22b	53.72	46.17	0.08	b.d.	b.d.	b.d.	0.20	0.14	0.01	b.d.	b.d.	b.d.	b.d.	0.03	100.38
23b	53.15	46.28	0.04	b.d.	b.d.	0.02	0.02	0.06	b.d.	b.d.	b.d.	b.d.	b.d.	0.03	99.61
24b	52.56	45.69	0.04	b.d.	0.02	98.33									
25b	52.81	45.78	0.04	b.d.	b.d.	b.d.	0.05	0.02	b.d.	b.d.	b.d.	b.d.	b.d.	0.03	98.72
27b	53.54	45.85	0.09	0.02	0.03	0.05	0.14	0.60	0.04	0.50	0.11	0.15	0.48	0.60	102.28
30b	53.44	45.84	0.07	b.d.	b.d.	b.d.	0.04	0.02	0.01	b.d.	b.d.	b.d.	b.d.	0.03	99.47
31b(T2)	53.60	46.66	0.03	b.d.	b.d.	0.02	b.d.	0.24	0.01	b.d.	b.d.	b.d.	b.d.	0.03	100.60
31b(T2)	53.35	46.37	0.04	0.21	b.d.	0.12	b.d.	0.61	b.d.	b.d.	b.d.	b.d.	0.02	0.04	100.76
31b(T2)	52.59	45.89	0.04	0.23	b.d.	0.13	b.d.	0.24	b.d.	b.d.	b.d.	b.d.	b.d.	0.03	99.14
31b(T2)	53.28	46.43	0.04	0.14	b.d.	0.09	b.d.	0.23	b.d.	b.d.	b.d.	b.d.	b.d.	0.03	100.23
31b(T2)	53.12	46.49	0.04	b.d.	b.d.	0.07	b.d.	0.46	b.d.	b.d.	b.d.	b.d.	0.02	0.04	100.23
31b(T2)	53.70	46.46	0.04	0.17	b.d.	0.05	b.d.	0.45	b.d.	b.d.	b.d.	b.d.	0.02	0.04	100.92
31b(T2)	53.17	46.77	0.05	b.d.	b.d.	0.03	b.d.	0.41	b.d.	b.d.	b.d.	b.d.	b.d.	0.02	100.45
31b(T2)	52.62	46.59	0.09	b.d.	b.d.	0.16	b.d.	0.18	b.d.	b.d.	b.d.	b.d.	b.d.	0.03	99.67
31b(T2)	53.18	46.34	0.10	b.d.	b.d.	0.13	0.14	0.08	b.d.	b.d.	b.d.	b.d.	b.d.	0.03	100.01
31b(T2)	52.78	45.82	0.04	1.34	b.d.	0.26	0.07	0.24	b.d.	b.d.	b.d.	b.d.	b.d.	0.04	100.59
31b(T2)	52.31	46.77	0.03	b.d.	b.d.	b.d.	b.d.	0.17	b.d.	b.d.	b.d.	b.d.	b.d.	0.03	99.31

32b(T3)	53.59	46.60	0.04	b.d.	b.d.	b.d.	b.d.	0.35	b.d.	b.d.	b.d.	b.d.	b.d.	0.03	100.61
32b(T3)	53.82	46.56	0.04	b.d.	b.d.	b.d.	b.d.	0.23	b.d.	b.d.	b.d.	b.d.	b.d.	0.04	100.68
32b(T3)	53.71	46.50	0.04	b.d.	b.d.	0.01	b.d.	0.19	b.d.	b.d.	b.d.	b.d.	b.d.	0.03	100.49
32b(T3)	53.45	46.22	0.04	b.d.	b.d.	0.02	b.d.	0.34	b.d.	b.d.	b.d.	b.d.	b.d.	0.04	100.12
32b(T3)	52.30	45.10	0.03	0.13	b.d.	0.05	0.26	0.23	b.d.	b.d.	b.d.	b.d.	0.02	0.04	98.17
32b(T3)	53.19	46.30	0.04	b.d.	b.d.	0.01	0.02	0.01	b.d.	b.d.	b.d.	b.d.	b.d.	0.04	99.61
32b(T3)	53.19	46.45	0.06	b.d.	b.d.	0.02	0.02	0.16	b.d.	b.d.	b.d.	b.d.	b.d.	0.03	99.93
32b(T3)	53.69	46.42	0.05	b.d.	b.d.	0.04	0.02	0.17	0.01	b.d.	b.d.	b.d.	b.d.	0.04	100.44
<i>PFI-45</i>															
33b(T4)	52.66	45.91	0.04	b.d.	b.d.	0.02	b.d.	0.23	0.01	b.d.	b.d.	b.d.	0.02	0.04	98.92
33b(T4)	53.44	46.61	0.05	b.d.	b.d.	b.d.	0.11	0.27	b.d.	b.d.	b.d.	b.d.	0.02	0.03	100.53
33b(T4)	53.27	45.62	0.05	b.d.	b.d.	0.04	0.76	0.15	b.d.	b.d.	b.d.	b.d.	0.03	0.05	99.97
33b(T4)	54.95	46.49	0.04	b.d.	b.d.	b.d.	b.d.	0.20	b.d.	0.02	b.d.	b.d.	0.05	0.06	101.80
34b	53.34	46.20	0.03	b.d.	b.d.	b.d.	b.d.	0.02	0.13	b.d.	b.d.	b.d.	b.d.	0.04	99.77
35b	53.40	45.63	0.05	b.d.	b.d.	0.01	0.41	0.17	b.d.	b.d.	b.d.	b.d.	0.02	0.05	99.75
36b	55.01	46.38	0.03	b.d.	b.d.	b.d.	b.d.	0.15	b.d.	b.d.	b.d.	b.d.	b.d.	0.04	101.62
40b	53.85	46.36	0.05	b.d.	b.d.	b.d.	b.d.	0.38	b.d.	b.d.	b.d.	b.d.	0.02	0.06	100.71
41b(T5)	53.06	46.30	0.03	b.d.	b.d.	0.01	b.d.	0.50	0.01	b.d.	b.d.	b.d.	b.d.	0.03	99.95
41b(T5)	52.29	45.78	0.03	b.d.	b.d.	b.d.	b.d.	0.29	b.d.	b.d.	b.d.	b.d.	0.03	0.05	98.46
41b(T5)	52.26	45.63	0.03	b.d.	b.d.	b.d.	b.d.	1.23	0.01	b.d.	b.d.	b.d.	0.03	0.05	99.24
41b(T5)	53.23	45.56	0.03	b.d.	b.d.	0.02	b.d.	1.46	0.02	0.02	b.d.	b.d.	0.03	0.06	100.42
41b(T5)	53.24	46.18	0.03	b.d.	b.d.	b.d.	b.d.	1.09	0.01	b.d.	b.d.	b.d.	0.02	0.04	100.62
41b(T5)	53.15	46.19	0.03	b.d.	b.d.	b.d.	b.d.	1.20	b.d.	b.d.	b.d.	b.d.	0.03	0.06	100.65
41b(T5)	53.42	45.75	0.03	b.d.	b.d.	b.d.	b.d.	0.07	0.74	b.d.	b.d.	b.d.	0.03	0.06	100.11
41b(T5)	53.09	45.86	0.03	b.d.	b.d.	b.d.	b.d.	1.12	b.d.	b.d.	b.d.	b.d.	0.02	0.06	100.19
41b(T5)	53.48	45.47	0.03	b.d.	b.d.	b.d.	b.d.	0.60	b.d.	b.d.	b.d.	b.d.	0.03	0.05	99.66
42b(T6)	53.73	46.41	0.03	b.d.	b.d.	b.d.	b.d.	0.12	b.d.	b.d.	b.d.	b.d.	0.02	0.04	100.35
42b(T6)	53.80	46.35	0.04	b.d.	b.d.	b.d.	b.d.	0.14	b.d.	b.d.	b.d.	b.d.	b.d.	0.03	100.35
42b(T6)	53.77	46.19	0.03	b.d.	b.d.	0.02	b.d.	0.02	0.01	b.d.	b.d.	b.d.	0.02	0.03	100.08
42b(T6)	53.09	46.15	0.03	b.d.	b.d.	b.d.	b.d.	0.83	0.01	b.d.	b.d.	b.d.	b.d.	0.04	100.16
42b(T6)	53.12	46.29	0.03	b.d.	b.d.	b.d.	b.d.	0.48	b.d.	b.d.	b.d.	b.d.	b.d.	0.03	99.95
42b(T6)	53.40	46.13	0.03	b.d.	b.d.	b.d.	b.d.	0.29	b.d.	b.d.	b.d.	b.d.	b.d.	0.03	99.88
42b(T6)	51.87	46.20	0.04	b.d.	b.d.	b.d.	b.d.	0.50	b.d.	b.d.	b.d.	b.d.	b.d.	0.04	98.61

Table 2

Secondary Ion Mass Spectrometry (SIMS) analyses of Au, Ag, Co, Cu, As, Sb, Se and Te in Pyrite from the Tolhuaca Geothermal System. Detection limits (DL) are shown in ppm.

DL	Au (ppm) 0.14	Ag (ppm) 0.38	Co (ppm) 0.28	Cu (ppm) 0.55	As (ppm) 1.62	Sb (ppm) 5.45	Se (ppm) 0.05	Te (ppm) 0.30
<i>PFI-2</i>								
01pycl31	0.40	2.21	10.3	444	24	b.d.	0.15	b.d.
01pycl33	b.d.	3.74	116	1123 ^a	226	22.7	b.d.	b.d.
01pycl35	b.d.	2.26	34.2	277	1132	36.2	b.d.	b.d.
01pycl38	b.d.	10.5	274	21	16347	6.33	0.53	b.d.
01pycl39	b.d.	4.05	141	837	384	23.5	b.d.	b.d.
01pycl40	b.d.	2.21	114	1091	206	13.8	0.15	b.d.
01pycl42	b.d.	6.33	105	553	14729	45.3	0.08	b.d.
01pycl44	0.17	6.53	101	472	11242	16.9	3.43	b.d.
01pycl48	b.d.	3.13	223	420	4535	34.0	b.d.	b.d.
01pycl50	b.d.	10.6 ^a	14.6	234	21647	35.0	0.95	b.d.
01pycl51	0.16	b.d.	13.4	71.4	244	b.d.	b.d.	b.d.
01pyp129	b.d.	1.25	73.3	862	839	22.4	0.10	b.d.
01pyp130	0.25	4.18	705	1425	158	7.98	0.13	b.d.
01pyp132	b.d.	7.20	261	1165	9887	58.4	0.48	b.d.
01pyp134	b.d.	10.4	426	5980	11565	88.0	0.43	b.d.
01pyp136	b.d.	6.98	457	3112	235	12.0	0.18	b.d.
01pyp137	b.d.	8.16	1173	2950	824	10.8	0.40	b.d.
01pyp141	b.d.	b.d.	1220	2243	288	b.d.	b.d.	b.d.
01pyp143	b.d.	7.77	653	2175	11187	71.1	0.40	b.d.
01pyp145	0.17	10.7	1544	2847	4484	47.6	1.70	b.d.
01pyp146	b.d.	4.72	247	1988	834	25.2	0.13	b.d.
01pyp147	b.d.	4.96	222	1490	2248	34.7	0.30	b.d.
01pyp149	b.d.	4.08	92.4	809	2246	55.7	b.d.	b.d.
<i>PFI-3</i>								
01pyc01	0.15	4.6	182	274.0	2136	24.9	1.33	1.35
01pyc06	3.58	30.9	5.7	3354.0	136	68.4	1.20	22.50
01pyc07	b.d.	1.04	243	422.0	1193	9.9	0.85	b.d.
01pyc08	b.d.	1.82	247	471.0	2805	41.0	0.55	b.d.
01pyc15	b.d.	3.45	423	1124.0	1893	54.8	1.18	b.d.
01pyc18	b.d.	b.d.	3.4	4.5	12.50	b.d.	14.30	0.88
01pyc19	b.d.	2.66	239	196.0	5355	28.9	2.68 ^a	0.33
01pyc22	b.d.	3.45	117	654.0	988	57.5	0.43	0.58
01pyc23	b.d.	1.44	136	323.0	3615	22.0	0.63	b.d.
01pyp02	0.15	3.51	900	2202.0	2925	81.9	2.70	b.d.
01pyp04	b.d.	4.84	406	1405.0	1505	59.4	3.20	0.90
01pyp05	15.4 ^a	5.54	6	3572.0	158	10.2	1.58	13.80
01pyp09	0.24	5.24	1055	3928.0	1817	94.1	5.93	0.30
01pyp10	0.43	5.66	669	1708.0	1963	80.9	2.45	0.58
01pyp12	0.26	4.86	823	5155.0	1303	76.3	3.03	b.d.
01pyp13	b.d.	1.78	199	1335.0	2727	74.4	0.88	1.08
01pyp14	b.d.	1.51	720	1202.0	2907	55.8	3.90	b.d.
01pyp16	4.63 ^a	1.32	7.9	4962.0	31.7	b.d.	1.60	0.60
01pyp17	b.d.	3.86	1292	3184.0	2440	44.6	2.38	b.d.
01pyp20	b.d.	1.52	304	461.0	4058	57.5	0.13	b.d.
01pyf03	0.28	7.54	120	296.0	672	40.9	0.75	1.55
01pyf11	b.d.	0.62	142	805.0	517	20.3	1.98	b.d.
01pyf21	0.19	2.35	147	448.0	490	29.5	0.83	0.38
<i>PFI-26</i>								
01pycl04	b.d.	b.d.	59.9	13.7	1346 ^a	b.d.	2.28	b.d.
01pycl17	b.d.	b.d.	168	186.0	834	b.d.	5.58	0.30
01pycl19	b.d.	b.d.	62.5	22.0	568	6.0	28,20 ^a	6.78
01pycl22	b.d.	b.d.	13.4	85.4	278	b.d.	12.20	1.13
01pycl27	b.d.	1.01	9.8	134.0	1670	49.6	1.03	b.d.
01pyp100	b.d.	b.d.	22.7	22.6	19.40	b.d.	34.60	b.d.
01pyp101	b.d.	0.61	47.6	33.7	1035	b.d.	18.70	b.d.
01pyp105	b.d.	1.87	53.8	24.3	115	b.d.	24.50	1.30
01pyp113	b.d.	0.8	1117 ^a	45.6	2033	19.5	2.00	b.d.

Table 2 (continued)

DL	Au (ppm) 0.14	Ag (ppm) 0.38	Co (ppm) 0.28	Cu (ppm) 0.55	As (ppm) 1.62	Sb (ppm) 5.45	Se (ppm) 0.05	Te (ppm) 0.30
01ypy114	b.d.	b.d.	40.8	30.7	402	b.d.	24.50	b.d.
01ypy115	b.d.	0.83	18.0	21.3	1923	8.88	7.28	b.d.
01ypy116	b.d.	0.51	43.3	30.5	651	b.d.	13.60	b.d.
01ypy118	b.d.	0.75	49.8	58.7	1155	b.d.	23.50	b.d.
01ypy120	b.d.	b.d.	73.3	17.7	131	b.d.	34.90	1.80
01ypy121	b.d.	0.54	43.6	38.9	1299	8.30	7.15	b.d.
01ypy123	b.d.	0.48	24.7	42.0	142	b.d.	17.40	0.70
01ypy126	0.20	2.52	561	149.0	3429	85.6	6.73	0.35
01ypy128	0.26	5.25	81	112.0	883	23.3	26.90	4.90
01pyf98	b.d.	0.85	84.6	35.7	211	12.65	15.20	b.d.
01pyf99	b.d.	b.d.	79.5	62.7	64.1	b.d.	20.60	b.d.
01pyf102	b.d.	b.d.	89.3	49.5	299	11.08	19.20	1.68
01pyf103	b.d.	b.d.	75.9	62.1	97.5	9.93	28.30	1.03
01pyf106	0.19	1.64	21.9	41.7	2196	15.33	1.05	b.d.
01pyf107	0.50	10.1	260	169.0	886	32.2	28.40	6.88 ^a
01pyf109	0.17	0.51	175	157.0	451	9.58	10.60	1.23
01pyf110	b.d.	0.65	140	68.4	420	b.d.	15.30	b.d.
01pyf111	b.d.	b.d.	99	56.3	469	12.9	15.30	1.88
01pyf112	b.d.	2.62	352	383.0	886	46.2	15.00	1.35
01pyf124	b.d.	0.51	147	235.0	193	13.8	9.63	1.10
01pym108	0.77	8.42	978	892.0	1099	118.0	12.50	6.98
01pym125	0.33	4.41	659	403.0	985	117.0	14.10	3.85
<i>PFI-4I</i>								
01pyc24	b.d.	b.d.	21.7	38.2	234	b.d.	0.13	b.d.
01pyc25	0.39	1.42	10.7	5.7	2792	b.d.	2.33	1.03
01pyc36	0.60	b.d.	149	2.5	133	b.d.	3.90	3.03
01pyc40	0.26	2.19	25.7	44.5	1535	112.0	1.28	b.d.
01pyc54	0.28	5.67	b.d.	3.6	11298	b.d.	1.83	b.d.
01ypy27	0.41	10.6	51.2	26.3	4441	99.1	2.00	3.83
01ypy28	0.52	4.31	210	55.4	3533	232.0	2.78	b.d.
01ypy30	0.15	2.13	276	102.0	1162	208.0	1.25	b.d.
01ypy38	0.54	3.05	192	115.0 ^a	4058	262.0	1.95	0.30
01ypy39	0.33	2.36	89.8	38.7	3124	156.0	2.13	b.d.
01ypy43	b.d.	1.27	317	53.4	1140	266.0	1.98	b.d.
01ypy49	0.14	1.05	87.2	58.7	857	174.0	2.18	b.d.
01ypy50	0.58	3.92	29.7	117.0	5355	6.18	6.98	b.d.
01ypy56	b.d.	2.03	217	94.7	1250	263.0	2.48	b.d.
01pyf26	b.d.	b.d.	257	67.8	5754	b.d.	b.d.	b.d.
01pyf29	0.44	4.82	315	161.0	3735	89.9	0.68	0.70
01pyf31	0.23	2.67	114	111.0	789	154.0 ^a	0.88	b.d.
01pyf32	b.d.	b.d.	287	163.0	730	b.d.	b.d.	b.d.
01pyf33	0.27	1.79	111	74.3	1616	33.3	0.45	b.d.
01pyf34	0.36	8.95	353	126.0	1082	57.3	0.58	1.43
01pyf35	0.46	3.54	219	196.0	2240	46.1	1.05	b.d.
01pyf37	1.27	6.6	1317	381.0	8390	178.0	5.98	b.d.
01pyf41	b.d.	b.d.	42.2	59.5	2715	b.d.	b.d.	b.d.
01pyf42	0.58	8.1	46.4	62.9	1938	62.2	1.08	7.15
01pyf44	0.47	6.04	633	273.0	3152	162.0	2.85	b.d.
01pyf45	0.27	3.88	218	289.0	3924	328.0	1.70	b.d.
01pyf46	0.35	2.24	207	84.9	1174	28.5	0.63	b.d.
01pyf47	0.25	1.56	83.1	35.5	1508	88.2	1.10	b.d.
01pyf48	0.38	5.32	127	62.9	336	26.1	0.13	1.00
01pyf51	0.47	5.31	323	272.0	4851	104.0	3.90	b.d.
01pyf52	0.35	4.83	361	75.9	6742	77.3	0.73	b.d.
01pyf53	b.d.	0.51	84.1	39.5	714	12.5	0.23	b.d.
01pyf55	b.d.	1.53	133	36.7	1910.0 ^a	b.d.	0.68	b.d.
<i>PFI-4S</i>								
01pyc57	b.d.	5.12 ^a	1.1	25.5	10617	265.0	0.05	b.d.
01pyc75	b.d.	3.49	50.4	50.2	5659	22.0	b.d.	b.d.
01pyc92	b.d.	5.59	7.5	22.2	10764	25.5	b.d.	b.d.
01pyc94	b.d.	6.32	9.1	37.2	11223	83.2	0.13	b.d.

(continued on next page)

Table 2 (continued)

DL	Au (ppm) 0.14	Ag (ppm) 0.38	Co (ppm) 0.28	Cu (ppm) 0.55	As (ppm) 1.62	Sb (ppm) 5.45	Se (ppm) 0.05	Te (ppm) 0.30
01pyc95	b.d.	3.58	19.8	29.8	7192	24.4	0.13	b.d.
01pyp59	b.d.	3.92	2.2	41.8	6971	44.6	0.13	b.d.
01pyp62	b.d.	1.89	21.7	18.2	3131	6.28	0.45	b.d.
01pyp70	b.d.	3.06	35.0	21.3	6379	6.9	0.68	b.d.
01pyp72	0.15	6.14	13.8	43.9	12718	41.1	0.98	b.d.
01pyp74	b.d.	1.83	17.2	18.3	4357	6.05	1.83	b.d.
01pyp78	b.d.	2.74	b.d.	61.1	5387	86.4	b.d.	b.d.
01pyp79	0.14	8.85	22.0	37.2	15756	58.2	0.75	b.d.
01pyp83	b.d.	6.69	1.4	4.8	12968	171.0	b.d.	b.d.
01pyp85	b.d.	3.67	25.0	29.7	6446	17.5	0.63	b.d.
01pyp86	b.d.	1.47	35.0	18.2	3002	b.d.	0.45	b.d.
01pyp90	b.d.	3.52	21.1	17.5	6377	12.2	1.00	b.d.
01pyf60	b.d.	7.14	196	105.0	10874	74.7	1.08	b.d.
01pyf63	0.15	5.91	87.7	116.0	8952	119.0	1.53	b.d.
01pyf64	b.d.	6.33	69.2	111.0	7983	47.4	1.15	b.d.
01pyf65	0.37	6.09	26.2	108.0	8741	80.4	1.15	b.d.
01pyf67	b.d.	1.39	103	54.2	2195	11.7	0.45	b.d.
01pyf69	0.16	5.74	49.4	46.1	9277	44.3	0.95	b.d.
01pyf71	b.d.	1.39	80	46.3	2443	19.5	0.33	b.d.
01pyf76	b.d.	2.53	74.3	77.2	2298	48.3	0.83	b.d.
01pyf80	b.d.	4.81	36.8	42.0	7464	13.3	1.78	b.d.
01pyf89	b.d.	3.04	127	63.7	6123	38.7	0.23	b.d.
01pyf91	b.d.	9.04	398	136.0	12162	139.0	1.20	b.d.
01pyf96	b.d.	4.56	42.2	57.7	8296	44.9	0.60	b.d.
01pyf98	b.d.	0.85	84.6	35.7	211	12.7	15.20	b.d.
01pym58	b.d.	3.20	50.7	148.0	1899	b.d.	5.15	b.d.
01pym61	0.33	11.02	507	698.0	5186	34.4	13.10	b.d.
01pym66	b.d.	2.94	105	276.0	3420	27.9	19.50	b.d.
01pym68	b.d.	7.50	36.5	70.7	15395	75.9	0.48	b.d.
01pym73	b.d.	4.17	55.8	171.0	2952	47.3	5.68	b.d.
01pym77	0.17	6.72	70.2	361.0	5661	40.2	25.00	b.d.
01pym81	0.23	3.79	31.0	158.0	1632	14.1	1.98	b.d.
01pym82	b.d.	3.37	44.3	159.0	6637	59.4	4.75	b.d.
01pym84	0.16	4.07	49.6	120.0	7587	4604.0	1.38	b.d.
01pym87	0.16	8.32	102	108.0	10171	50.7	0.70	0.50
01pym88	0.36	5.12	38.6	278.0	2321	16.7	12.80	b.d.
01pym93	0.33	9.50	29.3	293.0	4295	29.8	17.80	1.45
01pym97	0.30	3.25	68.2	170.0	2019	23.8	3.15	b.d.

^a Samples (and elements) that were depth-profile using SIMS.

atomic number background corrections were employed throughout (Donovan and Tingle, 1996). Unknown and standard intensities were corrected for dead time and the ZAF algorithm was used for matrix absorption (Armstrong, 1988). On-peak interference corrections were applied as appropriate (Donovan et al., 1993). Detection limits ranged from 0.006 wt.% for Sb to 0.032 wt.% for Au.

Wavelength-dispersive spectrometry (WDS) X-ray maps were acquired using the calibration set up described above. Detection limit maps were acquired for these elements and applied as the minimum cut-off values. Map acquisition utilized a 100 nA beam current with 2 × 2 μm pixel dimension and 40 ms dwell time per pixel. Data were processed using the Calcimage software package and output to Surfer® for further processing and enhancement.

Additionally, 152 secondary-ion mass spectrometry (SIMS) spot analyses were acquired on individual pyrite grains from selected samples from the argillic and propylitic

alteration zones (Table 2). SIMS analyses were performed at the Advanced Mineral Technology Laboratories (AMTEL) in London, Ontario, using a Cameca IMS-3f ion microprobe. Secondary ions monitored were ⁶³Cu, ⁶⁵Cu, ⁷⁵As, ⁷⁸Se, ⁸⁰Se, ¹⁰⁷Ag, ¹⁰⁹Ag, ¹²¹Sb, ¹²³Sb, ¹²⁸Te, ¹³⁰Te, and ¹⁹⁷Au. In addition, the major sulfide-matrix constituent isotopes, ⁵⁶Fe and ³⁴S were monitored. A 10 kV and 8 nA primary Cs + beam source was used for measurements, with a 4.5 kV accelerating voltage used for the negative secondary ions. The analytical spot size of the primary beam was ~25 μm; depth of analysis was 3.5–7.0 μm. Mineral standards used were produced experimentally by implanting a known dosage of the element of interest into the pyrite matrix using the Tandetron accelerator at the University of Western Ontario, Canada. The detection limits were ~0.03 ppm for Au, 3 ppm for As, 0.1 ppm for Cu, 0.02 ppm for Ag, 0.2 ppm for Sb, 0.01 ppm for Te, and 0.1 ppm for Se. For depth-concentration profiles, the mini-

mum detectable size of sub-micron mineral inclusions was 500 nm at a 5 s counting time. Thus, if more than one nanoparticle or inclusion is intercepted simultaneously, they register as a single particle in the depth profile.

4. RESULTS

Representative EPMA and SIMS analyses of pyrite are reported in Tables 1 and 2, respectively. A summary of the trace elements concentration in pyrite is presented in Fig. 3. Back-scattered electron (BSE) images and quantitative WDS X-ray maps of representative samples from the shallow argillic alteration zone (PFI-2 and PFI-3) are shown in Fig. 4, while Fig. 5 displays WDS X-ray maps of pyrite grains from the deeper propylitic alteration zone (PFI-39 and PFI-41). Although no marked vertical variation in the trace element concentrations was generally observed in pyrite from the TGS, the average concentrations of some metals (Cu, Co, Pb, and Ni) and metalloids (As, Sb, Te) are slightly higher in the shallower argillic alteration zone (first 250 m of the drillcore).

Pyrite from the TGS is characterized by high concentrations of As, Pb and Cu, up to ~5 wt.%, ~2 wt.% and ~1.5 wt.%, respectively (Fig. 3). Cobalt and Sb contents are also relatively high and vary from 0.2 to ~10,000 ppm and from ~0.3 to ~5000 ppm, respectively, spanning five orders of magnitude in concentration. Arsenic, Cu and Co show distinct zoning in the shallower argillic alteration zone (Fig. 4). WDS X-ray maps indicate that arsenic is enriched in the rims of pyrite crystals and depleted in the center (Fig. 4b, f, i, l, o and Fig. 5a and d), while Cu and Co show the opposite distribution with the highest concentrations found in the pyrite cores (Fig. 4c, d, g, j, k, m, n, p and q). WDS X-ray maps of fine-grained pyrite from the deeper, propylitic

alteration zone (Fig. 5a–f) do not display the well-defined zonation patterns observed in pyrite grains from the argillic alteration zone samples. Only one pyrite grain from the propylitic zone shows As-enriched cores (Fig. 5a), although these higher concentrations do not correlate with increased Cu or Co (Fig. 5b and c).

Concentrations of Au in pyrite are detectable using SIMS. Only one data point was detected by EPMA with a concentration of 1500 ppm (Table 1). SIMS data show Au values that vary between 0.01 to ~10 ppm. Silver concentrations range between 0.07 and ~400 ppm, with one data point reaching ~0.5 wt.%. Cadmium, Ti and Se contents of pyrite range from a minimum of 200, 160 and 0.03 ppm, respectively, to maximum concentrations of 1000's of ppm. Nickel and Te concentrations vary between ~60 and 600 ppm, and ~0.01 and 500 ppm, respectively.

5. DISCUSSION

5.1. Mineralogical incorporation of metals and metalloids in pyrite from the TGS

Pyrite from the TGS can be classified as “arsenian” in terms of its As contents (i.e., up to 5 wt.% levels), which is also in agreement with the high As concentrations documented in the well fluids and thermal springs (up to 25 ppm; Sánchez-Alfaro et al., 2016a). The generally homogeneous distribution of As in pyrite, as detected by WDS X-ray maps (Fig. 4b, f, i, l, o and Fig. 5a and d), strongly suggests that As is structurally bound (solid solution), even if the As–Fe–S ternary diagram in Fig. 6 suggests minor presence of As⁰. Correlation plots showing As–S and As–Fe inverse trends (Fig. 7a and b) and the ternary diagram of Fig. 6 does not show a conclusive trend of As substitution at the

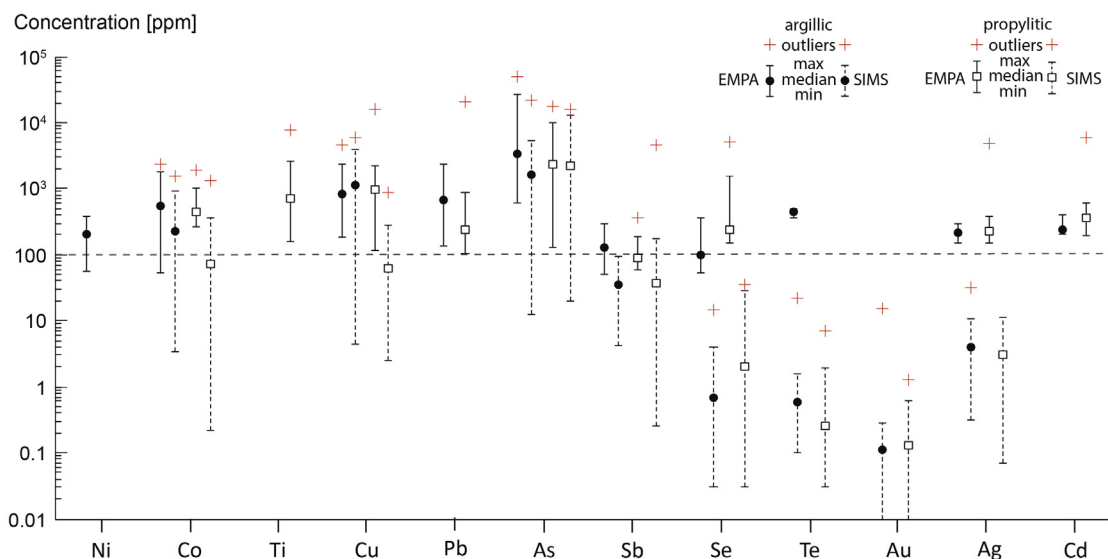


Fig. 3. Concentration plot for minor and trace elements in pyrite (samples PF-2, PF-3, PF-26, PF-39, PF-41 and PF-45). Pyrite data from argillic and propylitic alteration zones are identified by black circles and open squares, respectively. Data are plotted in parts per million (ppm) on a vertical logarithmic scale. For each element, median concentrations measured by EPMA (solid lines) and SIMS (segmented lines) are shown together with maximum and minimum values. Outliers are shown as red crosses. The horizontal dotted line is the mean detection limit (mdl) of EPMA analysis for all elements (~100 ppm).

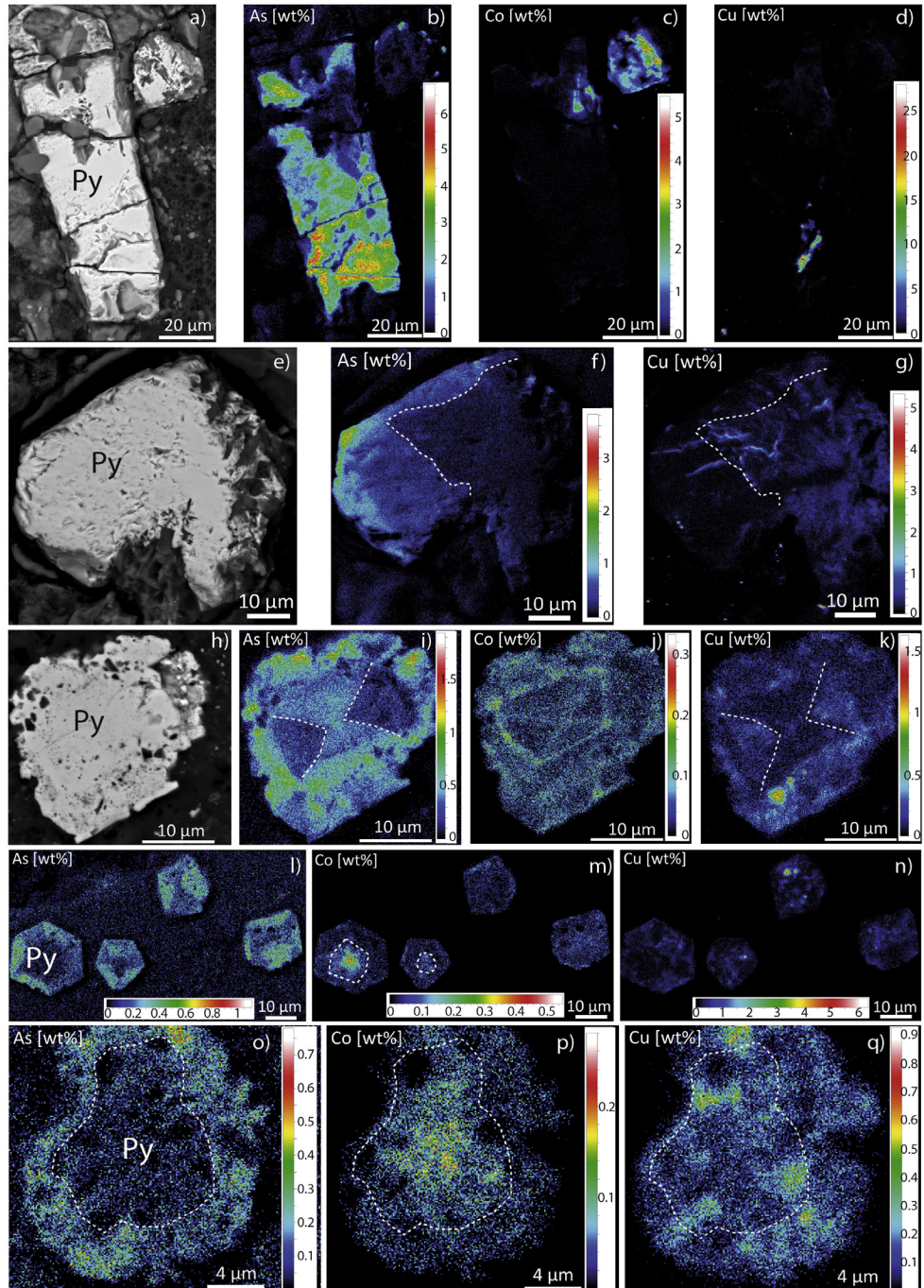


Fig. 4. Representative microtextures and chemical zonations of pyrite from the (shallow) argillic alteration zone of the Tolhuaca Geothermal System. Samples: PFI-2 (a–g) and PFI-3 (h–q). (a), (e) and (h): backscattered electron (BSE) image showing pyrite (Py) crystals. (b), (c), and (d): quantitative wavelength dispersive spectrometry (WDS) X-ray maps of area in (a) for As (K α), Co (K α), and Cu (K α), respectively. (f) and (g) Show WDX maps of area in (e) for As (L α) and Cu (K α), respectively. (i), (j) and (k) Show WDX maps of area in (h) for As (L α), Co (K α), and Cu (K α), respectively. (l) and (o); (m) and (p); and (n) and (q) show WDX maps of disseminated pyrite grains for As (L α), Co (K α), and Cu (K α), respectively. Quantitative WDX maps for As (L α), Co (K α), and Cu (K α) show zonations of these metals. Cu (K α) distributions in (d), (k) and (n) show discrete inclusions of chalcopyrite. A color scale bar for concentration (in wt.%) is shown for each WDS map. Py: pyrite. (For interpretation of the references to colour in this figure legend, the reader is referred to the web version of this article.)

TGS, and it is likely that As¹⁻, As²⁺ and As³⁺ ionic species are present (Deditius et al., 2008, 2014; Qian et al., 2013). No significant clustering distribution of As are observed

in WDS maps, where As is markedly enriched in the pyrite rims (Fig. 4b, f, i, l and o). Also, no noticeable differences in As speciation are observed in pyrite from the shallower or

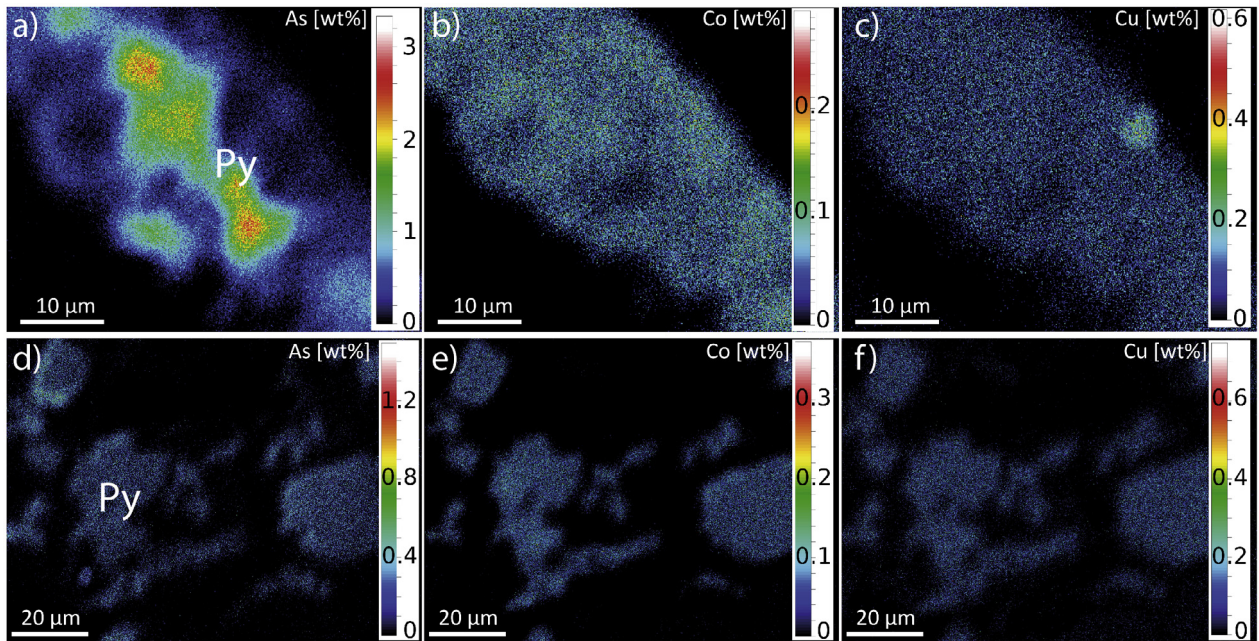


Fig. 5. Representative microtextures and chemical features of pyrite from the deep (propylitic) alteration zone. Samples: PFI-39 (a–c) and PFI-41 (d–f). (a) and (d) show quantitative WDX maps for As. (b) and (e) show maps for Co ($K\alpha$). (c) and (f) Show WDX maps for Cu ($K\alpha$). Cu ($K\alpha$) distribution in (c) shows discrete inclusions of chalcopyrite. Color scale bars for concentration (in wt.%) are shown. Py: pyrite. (For interpretation of the references to colour in this figure legend, the reader is referred to the web version of this article.)

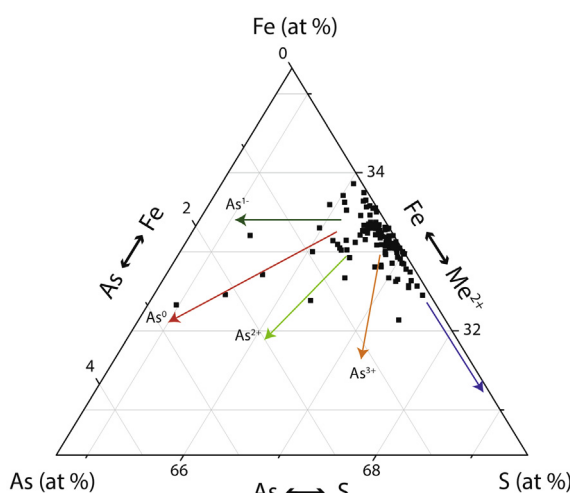


Fig. 6. Ternary diagram showing the As–Fe–S composition of pyrite in the Tolhuaca Geothermal System. Five different trends show substitution of (i) As for S (As^{1-} -pyrite; green arrow); (ii) As^0 nano-inclusions (As^0 red arrow); (iii) As^{2+} for Fe (As^{2+} -pyrite; light green arrow); (iv) As^{3+} for Fe (As^{3+} -pyrite; orange arrow); and (v) divalent metals Me^{2+} for Fe (blue arrow). The composition of As^{2+} -pyrite (after Qian et al., 2013; Deditius et al., 2014) was calculated based on the assumption of ideal occupancy of S (66.66 at.%). $n = 2924$. (For interpretation of the references to colour in this figure legend, the reader is referred to the web version of this article.)

deeper zones, as suggested using SIMS depth profiling, where each successively deeper layer of the material is analyzed as a function of time. The flat ^{75}As depth profile in

Fig. 8b strongly suggests that As is mainly incorporated within the pyrite structure.

The high Cu concentrations (up to ~2 wt.%) measured by EMPA are related to two dominant mineralogical forms of Cu, as observed on SIMS depth profiles: (i) structurally bound Cu, and (ii) as micro- to nano-sized inclusions of chalcopyrite (Fig. 8c and d). Both forms of Cu can also be observed in the elemental maps in Figs. 4d, g, k, n and q, and in Fig. 5c and f. Structurally bound Cu is distributed homogeneously, forming the light blue-colored areas usually restricted to the core of the pyrite crystals, which contrasts with the dark-blue, low-Cu background (Fig. 4d, g and k, WDS maps). The elemental plot in Fig. 7c shows a negative correspondence between Cu and Fe ($R^2 = 0.60$), suggesting $Cu^{2+} \leftrightarrow Fe^{2+}$ as a possible substitution, although the precise mechanism of Cu incorporation cannot be deduced (Shimazaki and Clark, 1970; Schmid-Burmann and Bente, 1995). It is likely that most of the structurally bound Cu replaces Fe in octahedral sites, which may be due to considerable distortion of the pyrite symmetry by the presence of other elements such as As, Sb or Co (Radcliffe and McSween, 1969; Bayliss, 1989).

Micro- to nano-sized Cu-bearing inclusions occur as scattered discrete particles and blebs along the growth zones (Fig. 4d, k, n and Fig. 5c; yellow-to-red-colored). The size of the particles is less than 5 μm , and they occur as individual inclusions and/or as aggregates of abundant micrometer- to submicrometer-sized particles. The occurrence of the two mineralogical forms of Cu in pyrite in the TGS is confirmed by SIMS depth profiling. In Fig. 8c and d, depth-concentration profiles are presented for the pyrite matrix isotopes (^{56}Fe , ^{34}S) and copper

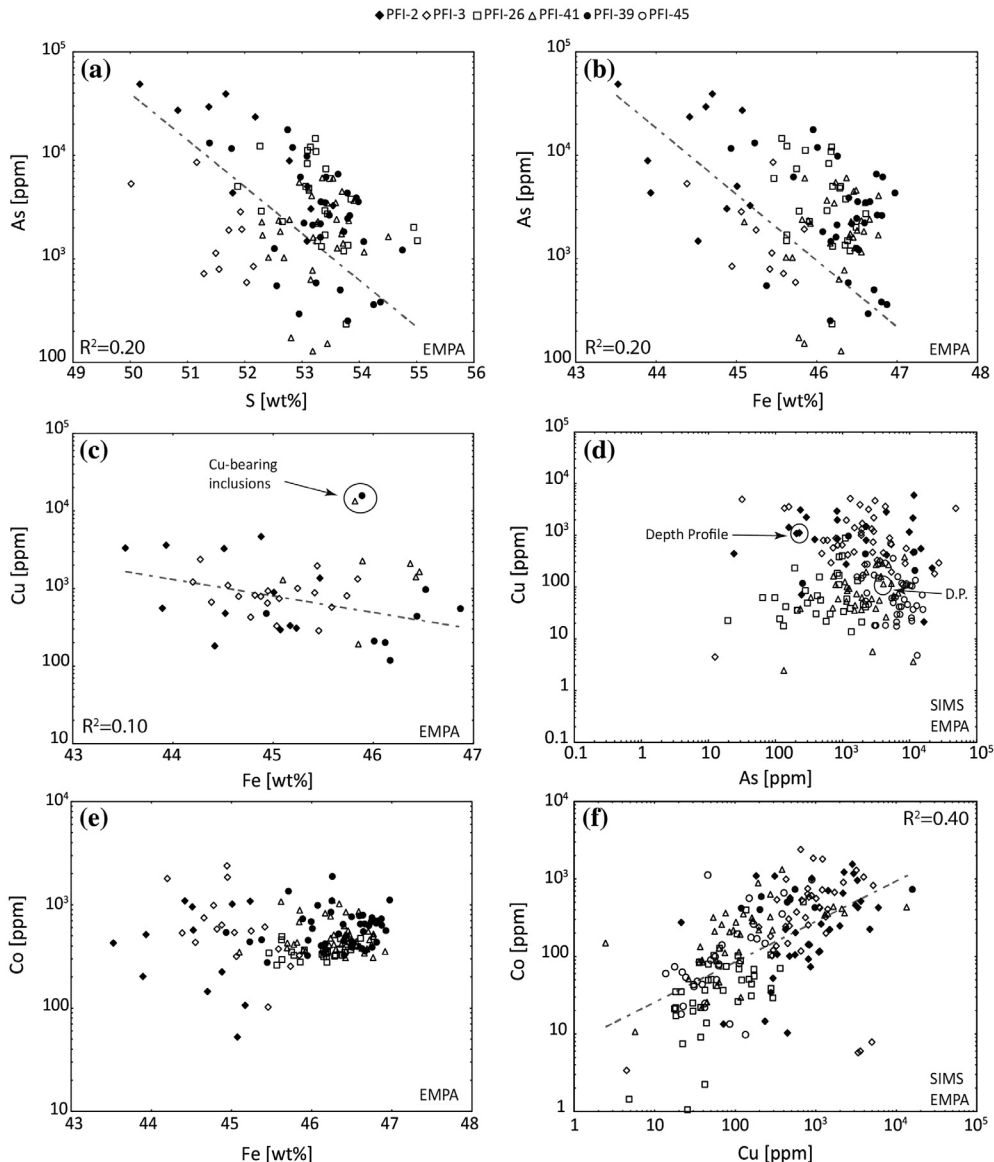


Fig. 7. Elemental correlation plots of (a) As vs. S, (b) As vs. Fe, (c) Cu vs. Fe, (d) Cu vs. As, (e) Co vs. Fe, and (f) Co vs. Cu. Black diamonds, open diamonds, open squares, open triangles, black circles and open circles represents pyrite samples PFI-2, PFI-3, PFI, 26, PFI, 39, PFI, 41 and PFI-45, respectively. R^2 values are shown.

(^{63}Cu). When Cu is present in solid solution (structurally bound), the depth-concentration profile of ^{63}Cu is flat (Fig. 8c, 1100 ppm Cu), whereas at higher concentrations the spiky ^{63}Cu profile confirms the presence of individual particles or clusters of particles of 500 nm in size (Fig. 8d, ~100 ppm Cu). Previous experimental studies have pointed out that the solid solution of CuS_2 in FeS_2 is thermodynamically unstable in nature and the solubility of Cu in FeS_2 decreases considerably with temperature (from 4.5 mol% Cu at 900 °C to ~0.6 mol% Cu at 700 °C, at 45 kbar; Shimazaki and Clark, 1970; Schmid-Beurmann and Bente, 1995). However, the solubility of Cu in pyrite has not been

determined at the lower temperatures relevant for most hydrothermal systems (e.g., <500 °C). Analogously to Reich et al. (2005), it may be suggested that the incorporation of As could influence Cu incorporation in both solid solution and as Cu-bearing nanoparticles in pyrite (Reich et al., 2013). At the TGS, Cu and As concentrations do not show a correspondence (Fig. 7d), and the micrometric chalcopyrite inclusions are found associated with both low and high As-bearing concentration zones. At very low temperatures (i.e., sedimentary settings) Cu is incorporated within the pyrite structure at low concentrations (ppm levels), while Cu-bearing microinclusions at present at

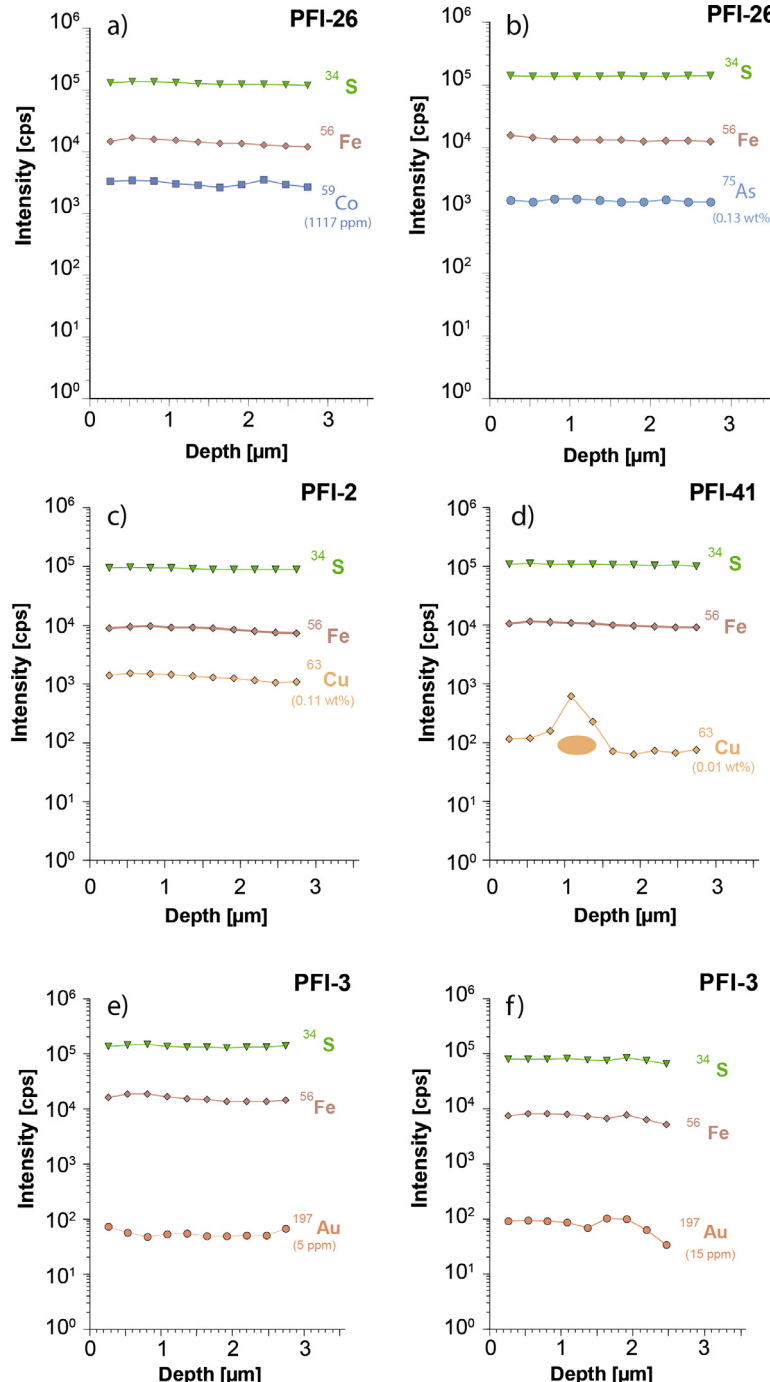


Fig. 8. SIMS depth-concentration profiles (time vs. intensity) of trace elements in pyrite from Tolhuaca Geothermal System. Spiky profiles for ^{63}Cu (c and d) reflect the presence of individual nanoinclusions or clusters of mineral nanoparticles (colored circles and ovals), whereas ^{59}Co (a), ^{75}As (b), and ^{197}Au (e and f) show a more homogeneous (solid-solution) distribution. Major sulfide-matrix constituent isotopes, ^{56}Fe and ^{34}S , were monitored during each run (top). Vertical intensity scale is in counts per second (cps); horizontal (depth) scale is in micrometers (μm). (For interpretation of the references to colour in this figure legend, the reader is referred to the web version of this article.)

higher concentrations (wt% levels; Gregory et al., 2015a). Factor analysis has shown that Cu is associated with large cations that disrupt the pyrite structure enhancing Cu incorporation. However, it is likely that the total concentration of the metals in fluids play a key role on Cu incorporation into pyrite as evidenced in studies such as Gregory et al. (2015a).

As shown in Tables 1 and 2 and Fig. 3, Co concentrations in pyrite are variable, ranging from hundreds of ppb to thousands of ppm. Despite the fact that the plot of Co-Fe in Fig. 7e does not show a clear correlation trend, the SIMS depth profile (Fig. 8a) and WDS X-ray maps (Fig. 4c, j, m and p) suggest that cobalt in the studied pyrites is in solid solution. This is in agreement with the fact

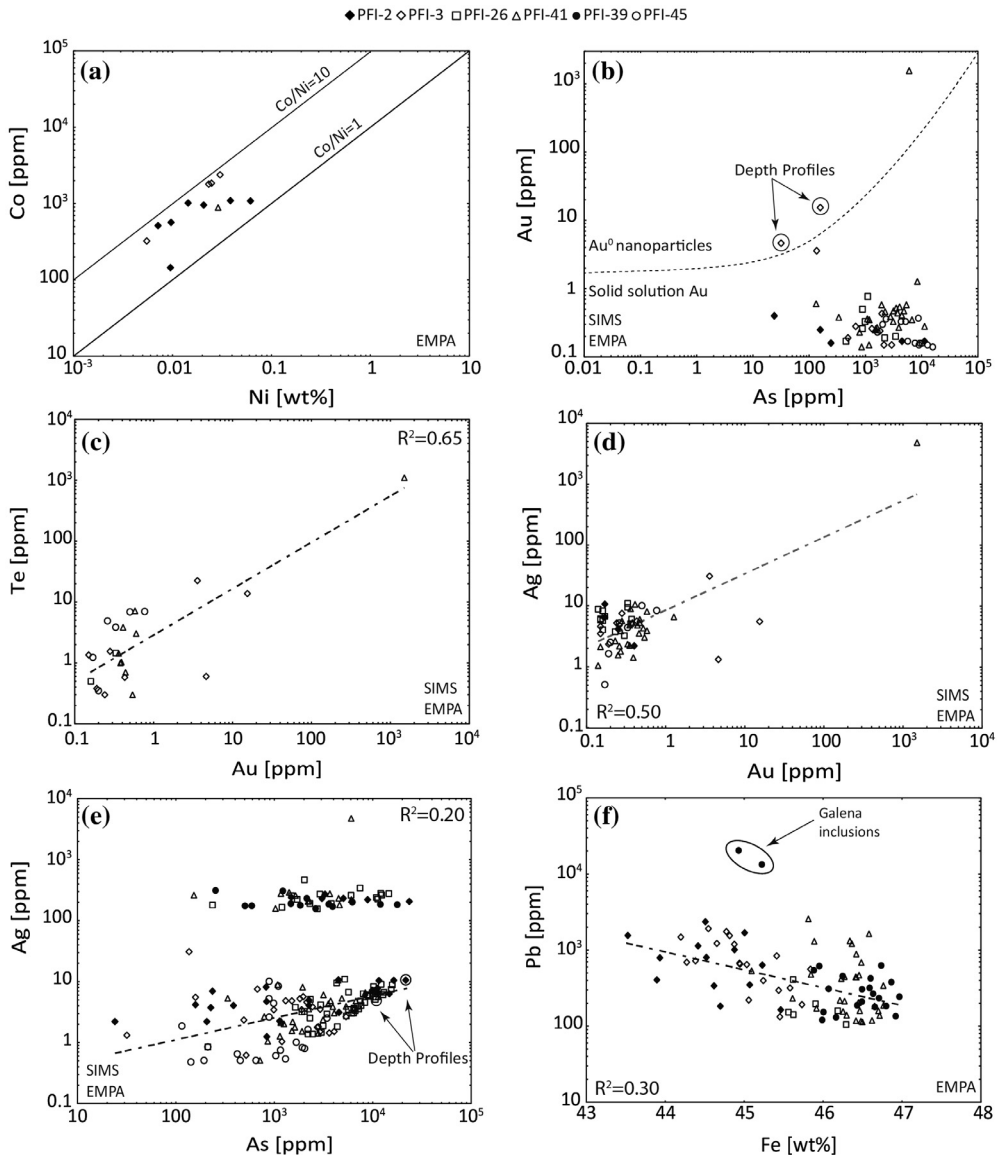


Fig. 9. Elemental correlation plots of (a) Co vs. Ni, (b) Au vs. As, (c) Te vs. Au, (d) Ag vs. Au, (e) Ag vs. As and (f) Pb vs. Fe. Black diamonds, open diamonds, open squares, open triangles, black circles and open circles represents pyrite samples PFI-2, PFI-3, PFI, 26, PFI, 39, PFI, 41 and PFI-45, respectively. Solid lines in (a) represent $\text{Co}/\text{Ni} = 1$ and $\text{Co}/\text{Ni} = 10$. The curve in (b) is the As-dependent solubility of Au in pyrite as determined by Reich et al. (2005). R^2 values are shown.

that Co extensively substitutes for Fe in pyrite, due to the similar ionic radii of Co^{2+} and Fe^{2+} , and that the CoS_2 end-member adopts the pyrite structure (Vaughan and Craig, 1978; Tossell et al., 1981; Abraites et al., 2004; Gregory et al., 2015a,b). WDS X-ray maps in Fig. 4c, j, n, p, show that chemical zoning of Co, like Cu, is spatially correlated to cores and/or thin bands within pyrite crystals. The positive correspondence between Co and Cu in Fig. 7f supports the hypothesis that these two metals may be included in pyrite in similar mineralogical form. The relatively high Co concentrations (up to ~ 0.2 wt.%) and high Co/Ni ratios between 1 and 10 in pyrite from the TGS (Fig. 9a) are indicative of a magmatic–hydrothermal origin associated

with a greater mafic affinity (Large et al., 2009; Koglin et al., 2010; Reich et al., 2016, 2017), in agreement with the composition of the lavas from Tolhuaca volcano, which have mainly basaltic to andesitic compositions (Sánchez-Alfarro et al., 2016a).

Apart from the base metals, precious metal (Au, Ag) concentrations in the studied pyrite are at least one order of magnitude higher when compared to pyrite from other active geothermal systems (Libbey and Williams-Jones, 2016), ranging from 0.01's to 10's of ppm for Au and from 0.01's to 1000's of ppm for Ag (Tables 1 and 2). Gold and silver incorporation into pyrite structure is favored by the substitution of anionic or cationic As, due to a structural

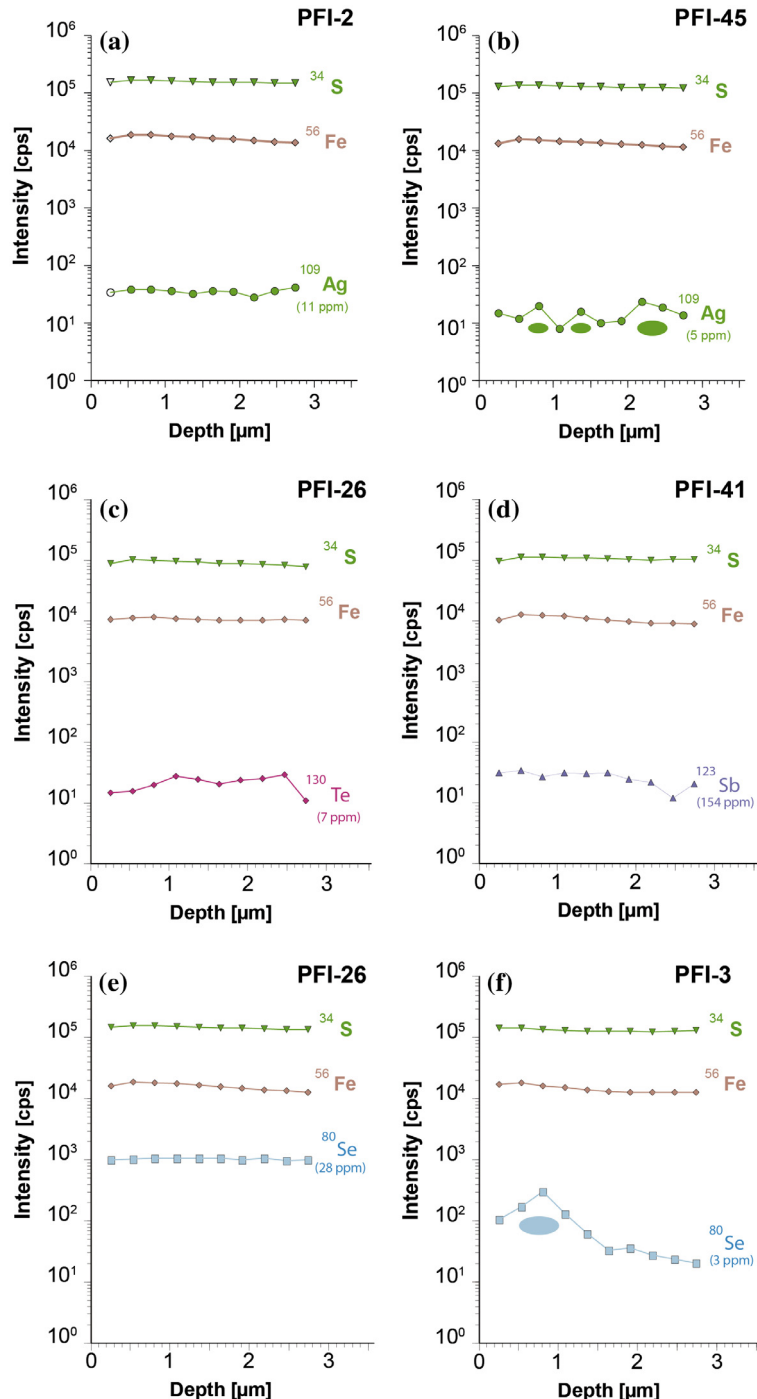


Fig. 10. SIMS depth-concentration profiles (time vs. intensity) of trace elements in pyrite from the TGS. Spiky profiles for ^{109}Ag (a and b), and ^{80}Se (e and f) reflect presence of individual nanoinclusions or clusters of mineral nanoparticles (colored circles and ovals), whereas ^{130}Te (c) and ^{123}Sb (d) show a more homogeneous (solid-solution) distribution. Major sulfide-matrix constituent isotopes, ^{56}Fe and ^{34}S , were monitored (top). Vertical intensity scale is in counts per second (cps); horizontal (depth) scale is in micrometers (μm). (For interpretation of the references to colour in this figure legend, the reader is referred to the web version of this article.)

distortion and/or decrease in the size of pyrite grains, increasing the surface/volume ratio (e.g., Simon et al., 1999; Palenik et al., 2004; Deditius et al., 2008, 2014). Several different incorporation mechanisms for Au and As

have been proposed for pyrite. The most validated model involves the coupled substitution of cationic Au for Fe in distorted octahedral sites and anionic As for S in tetrahedral sites (Simon et al., 1999). It is relevant to note that

the highest concentrations of Au in pyrite are usually related to the presence of Au-bearing micro- to nano-sized inclusions and clusters of Au nanoparticles (Reich et al., 2005; Deditius et al., 2014; Gregory et al., 2015a, 2016).

As shown in Table 2 and Fig. 3, SIMS data show Au concentrations in pyrite that varies between 0.01 and ~10 ppm. Only one EMPA data point reported in Table 1 shows Au concentration of 1500 ppm (sample PFI-41; Table 1). In Fig. 9b, most Au–As analyses plot below the solubility limit defined by Reich et al. (2005), suggesting that Au occurs as structurally bound ions (Au^{1+}). Only three data points plot above the As-dependent solubility limit, indicating the presence of nanoparticles of native Au^0 and/or Au-tellurides. Although SIMS depth-concentration profiles do not confirm the presence of nanoinclusions (Fig. 8e and f), the occurrence of nanoparticles smaller than the SIMS depth-profiling detection capabilities (<500 nm) is possible, and higher concentrations of Au (e.g., >10 ppm) measured by EMPA and SIMS may be related to micro- to nano-sized Au-bearing mineral particles. The similar incorporation behavior of Au and Te, both as solid solution or gold-telluride, is also assessed by the positive correlation between Au and Te, shown in Fig. 9c.

As shown in Tables 1 and 2 and summarized in Fig. 3, the measured Ag content of pyrite varies between ~0.07 and 5000 ppm. Previous studies have shown that Ag is widely present in pyrite in both solid solution (replacing Fe^{2+} as Ag^+) and/or forming micro and nano-sized Ag-sulfide and sulfosalt inclusions (Abrafitis et al., 2004; Deditius et al., 2011). At the TGS, SIMS depth profiles show that Ag occurs in both mineralogical forms. In Fig. 10a and b, depth-concentration profiles are presented for ^{109}Ag . The flat profile in Fig. 10a (at 11 ppm Ag) support the presence of Ag in solid solution, whereas the spiky ^{109}Ag profile confirms the presence of individual particles or clusters of Ag-bearing particles <500 nm in size (Fig. 10b, 5 ppm Ag). The generally positive trend between Ag and Au (Fig. 9d) suggests a similar incorporation behavior of these two metals, as documented in previous studies (e.g., Reich et al., 2010). Furthermore, Ag–As data points in Fig. 9e show two groups at higher (~200 ppm) and lower (<100 ppm) Ag contents. The lower Ag concentration group display a positive correspondence with As, while the high-Ag concentrations do not vary with As contents, showing a line parallel to the Y axis. These data, in addition to SIMS depth profiles in Fig. 10a and b, suggest that Ag incorporation into pyrite is dependent on As and follow a similar behavior than Au (Reich et al., 2005, 2013; Deditius et al., 2014).

All other trace elements measured in pyrite at the TGS (e.g. Pb, Ni, Ti, Sb, Se, Te, Cd) also occur in relatively high amounts, e.g., 100-ppm levels for Ni and Te, 1000-ppm levels for Ti, Sb, Se and Cd, and up to wt.% levels for Pb. Lead may be incorporated in solid solution by the substitution of Pb^{2+} for Fe^{2+} , as suggested by the negative relation shown in the elemental plot of Fig. 9f. However, the high concentrations of Pb (up to 2 wt.%) may also be attributed to the presence of sub-micron sized Pb-bearing inclusions, most likely galena (Griffin et al., 1991; Huston

et al., 1995; Abrafitis et al., 2004; Pacevski et al., 2012; Gregory et al., 2015a). Tellurium and Se are likely hosted in solid solution, as shown in the flat SIMS profiles (Fig. 10c and d), although the presence of micro- or nano-inclusions cannot be excluded. In fact, the SIMS depth profiles in Fig. 10e and f indicate that Se is probably incorporated in pyrite as both solid solution and Se-bearing mineral inclusions.

5.2. Decoupling of Cu and As in the TGS: linking pyrite chemistry with paleofluid and borehole fluid composition

The trace element geochemistry of pyrite has proven useful in accessing the history of complex processes undergone by a single sample. In magmatic–hydrothermal settings, pyrite has been used to fingerprint ore sources, vector towards mineralization and infer changes in fluid composition (e.g., Franchini et al., 2015; Mukherjee and Large, 2017). Similar observations are reported in lower temperature sedimentary environments where pore waters progressively enrich in trace elements as they desorb from organic matter, resulting in a sequential enrichment of trace elements in pyrite with increasing sediment depth (Huerta-Diaz and Morse, 1992; Gregory et al., 2014).

Abrupt changes in As and Cu concentrations in pyrite growth zones have been observed in the Pueblo Viejo and

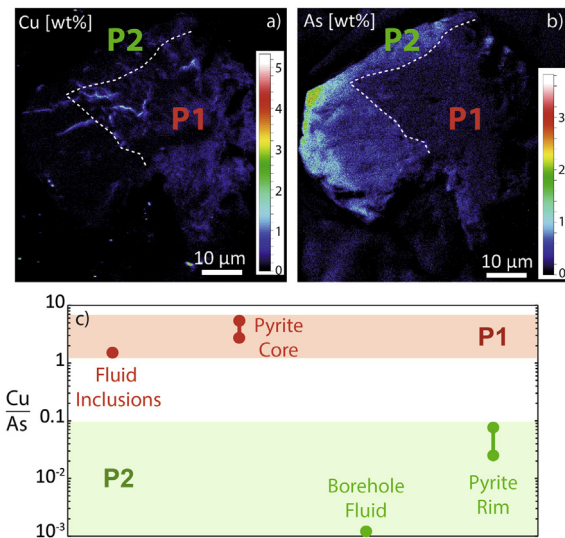


Fig. 11. Combination of pyrite data (WDS X-ray maps) with LA-ICP-MS analyses of fluid inclusions in pyrite-bearing veins and borehole fluids chemical data at the TGS. The panels (a) and (b) show a pyrite grain from the argillic zone that contains a Cu-rich, As-poor core (P1), and an As-rich, Cu-poor rim (P2). The panels (c) shows the Cu/As ratio of fluid inclusions (red circles) and borehole fluids samples (green circles), respectively, reported by Sánchez-Alfarro et al. (2016a). The Cu-rich, As-poor pyrite core (P1) correlates with the high Cu/As ratios measured in fluid inclusions in calcite-quartz-pyrite veins. Conversely, As-rich and Cu-poor pyrite rims (P2) correlate with the low Cu/As ratio measured in the present-day borehole fluid. (For interpretation of the references to colour in this figure legend, the reader is referred to the web version of this article.)

Yanacocha high sulfidation Au-Ag deposits (Deditius et al., 2009a,b). Arsenic-rich zones, also enriched in Au, Ag, Sb, Te, and Pb, alternate with Cu-rich zones with significantly lower concentrations of these elements and barren pyrite zones with no other elements. In situ trace element and sulfur isotope ($\delta^{34}\text{S}$) data by Peterson and Mavrogenes (2014) in pyrite at the Porgera Au deposit in Papua New Guinea uncovered a stratigraphy of repeated high-Au negative $\delta^{34}\text{S}$ and low-Au positive $\delta^{34}\text{S}$ zones, recognized with a 3 μm spot size laser ablation, within individual pyrite crystals present in the highest grade gold event. These zonations are less likely to reflect changes in substitutional mechanisms of As and Cu into pyrite forming from a fluid of constant composition. Rather, the chemical and isotopic data provide strong evidence pointing to sharp variations in the pyrite-forming fluid composition (Deditius et al., 2009a,b; Kouzmanov et al., 2010).

In high-temperature hydrothermal settings, these abrupt chemical changes have been interpreted as the result of mixing between the pyrite-forming fluids and magmatic vapors, the latter capable of geochemically decoupling As and Cu during its separation from the parental magma (Deditius et al., 2009a,b). Indeed, although it has been observed that both As and Cu partition into the magmatic vapor, they respond differently to P-T-X conditions of the system, especially in terms of ligands (Cl and S) availability (Heinrich et al., 1999, 2004; Pokrovski et al., 2002, 2005; Williams-Jones et al., 2002; Williams-Jones and Heinrich, 2005; Simon et al., 2006, 2007; Pokrovski et al., 2013). Magmatic vapors, formed by direct separation from the parental silicate magma, may remain a single phase or separate into a brine and a lower density vapor, a process that can take place more than once during the upward migration of the magmatic vapor (Heinrich et al., 2004, 2005). These phase separation processes are capable of fractionating As and Cu in the porphyry-epithermal environment. Pokrovski et al. (2005, 2013) compiled experimental data of vapor-liquid partition coefficients between 300 and 450 °C for various metalloids, base and precious metals. They determined that As partitions preferentially into the low density, low salinity vapor phase than Cu which has a higher affinity for the high-density saline brine. This selective metal partitioning has been extensively reported in experiments and fluid inclusion studies in ore deposits, from the deeper magmatic-hydrothermal porphyry roots to the shallower epithermal domain (Kouzmanov and Pokrovski, 2012, and references therein).

For most hydrothermal systems it remains difficult to determine how the compositions of hydrothermal fluids change with time and how those changes affect the precipitation of ore minerals, including pyrite (Rusk et al., 2008). Several studies have reported LA-ICP-MS data of fluid inclusions from porphyry systems (e.g., Heinrich et al., 2005; Audetat et al., 2008), epithermal Au(-Ag) deposits (e.g., Pudack et al., 2009), and from fluid inclusions hosted in sulfide ore minerals (e.g., Wilkinson et al., 2009; Kouzmanov et al., 2010). All these studies have reported significant variations in metal concentrations related to chemical fluctuation of hydrothermal ore fluids. Despite such evidence, a direct correlation between chemi-

cal changes in ore-forming fluids and the trace metal chemical zonations recorded in pyrite (e.g. Cu, As, Co, Au, Sb, Ni) remains to be confirmed beyond trace element analyses of the sulfide phase (Large et al., 2009; Deditius et al., 2009a,b; Thomas et al., 2011; Reich et al., 2013; Reich et al., 2016, 2017; Peterson and Mavrogenes, 2014; Deditius et al., 2014; Steadman et al., 2015; Gregory et al., 2016).

By combining our EMPA/SIMS pyrite data with (1) LA-ICP-MS analyses of fluid inclusion that are paragenetically linked in calcite/quartz veins, and (2) borehole fluid chemical data at the TGS, we provide evidence that the observed zonations in pyrite are likely related to chemical changes in the pyrite-forming hydrothermal fluid. Borehole fluids in the TGS have trace metal contents that are broadly similar to those measured in the Taupo Volcanic Zone in New Zealand and in the active Lihir gold deposit in Papua New Guinea (Simmons and Browne, 2000; Simmons et al., 2016a,b; Sánchez-Alfaro et al., 2016b). Furthermore, and unlike pyrites from ore deposits that commonly show multiple growth bands and complex oscillatory zoning patterns, pyrite in the shallow argillic zone of the TGS presents the advantage of having only two growth zones as observed in the WDS X-ray maps (Figs. 4 and 11).

The fluid inclusions data used in this study were reported by Sánchez-Alfaro et al. (2016a). In particular, the LA-ICP-MS data were obtained in fluid inclusion assemblages observed in pyrite-bearing, calcite/quartz veins retrieved from the shallower part of the drillcore (first 400 m), which represents the upwelling paleo-hydrothermal fluid. In contrast, the present-day borehole fluid composition (measured using ICP-MS) is likely to represent the resulting fluid after the condensation of a low-density vapor that separated from a magmatic-hydrothermal fluid sourced in the deeper parts of the hydrothermal system. This distinction allows us to correlate the composition of paleo- and present-day fluids with measured concentrations of trace metals in cores and rims of pyrite in the shallow argillic zone, which are the only pyrite grains that show clear zonation patterns.

As shown in Fig. 11a and b, we will refer in the following discussion to the pyrite growth zones as P1 for pyrite cores, and P2 for the pyrite rims. Copper-As ratios of pyrite cores (red) and rims (green) are compared in Fig. 11c with the Cu/As ratios of fluid inclusions (red circles) and borehole fluid from the TGS (green circles). The textural and chemical data in Fig. 11 suggest that a Cu-rich, As-depleted fluid was involved in pyrite core formation (P1), followed by a late-stage, low-Cu and high-As fluid related to the precipitation of pyrite rims (P2). In the same way, the comparison between (present-day) borehole fluids and fluid inclusion data reveals significant differences. Fluid inclusions are Cu-rich but poor in As (Cu/As ~1) while borehole fluids are rich in As, but Cu-poor (Cu/As ~10⁻³). According to Sánchez-Alfaro et al. (2016a), simple boiling models cannot explain the aforementioned differences in fluid chemistry because non-volatile elements such as Cu and As remain in the liquid phase during boiling ($K_d = C_{\text{vapor}}/C_{\text{liquid}}$, $K_{\text{As}} = 0.001-0.01$; $K_{\text{Cu}} < 10^{-3}$; $K_{\text{Na}} < 10^{-3}$) under epithermal conditions (100 < T < 280 °C; Pokrovski et al., 2013).

In Fig. 11, the relatively high-Cu, low-As concentrations in fluid inclusions ($\text{Cu}/\text{As} \sim 1$, Fig. 11c) can be paragenetically linked to the formation of the Cu-rich, As-depleted pyrite cores ($\text{Cu}/\text{As} \sim 1\text{--}10$, Fig. 11c). In contrast, the As-rich, Cu-depleted pyrite rims ($\text{Cu}/\text{As} \sim 0.1\text{--}0.01$, Fig. 11c) correlate with the high-As and low-Cu concentrations measured in the borehole fluid ($\text{Cu}/\text{As} \sim 10^{-3}$, Fig. 11c) at the TGS. These observations strongly suggest that the zonations reported in pyrite from TGS are the result of a compositional change of the pyrite-forming hydrothermal fluid during continuous pyrite precipitation.

EMPA data and WDS X-ray maps also show that pyrite cores are significantly enriched in Co (up to 4 wt.%). Unfortunately, no experimental partitioning data are available for Co, and Sánchez-Alfaro et al. (2016a) do not report Co concentrations in fluid inclusion or borehole fluids. However, and as shown by Pokrovski et al. (2013), most base metals present a marked affinity for a high-density saline brine; therefore it is reasonable to assume that Co may display a similar behavior than Cu (see maps in Fig. 4c, j, m and p).

The pyrite core precipitation stage P1 at Tolhuaca was most likely related to Cu(Co)-rich supercritical magmatic vapors that segregated during a stage of magmatic diking and sill intrusion as reported for the TGS. The episodic separation of these magmatic vapors produced fluid overpressure conditions inducing fracturing and brecciation of the low permeability clay-cap, as observed by Sánchez-Alfaro et al. (2016a). This magmatically derived single-phase fluid ascended, and following phase separation (or boiling) (Sánchez-Alfaro et al., 2016b), precipitated pyrite (cores) with high concentrations of Cu and Co, in both the deep and shallower parts of the TGS. Pyrite in the argillic (shallower) zone hosts higher concentrations of Cu and Co than pyrite in the propylitic (deeper) zone (Fig. 3; Tables 1 and 2). This may be due to the neutralization of acid hydrothermal fluids in the upper argillic zone, as proposed by Sánchez-Alfaro et al. (2016a), producing a concomitant decrease of metal solubility in the fluid phase.

During a later phase of evolution of the TGS (P2), the fluid pressure was lower than the lithostatic pressure and the clay-cap acted as a low-permeability barrier (Sánchez-Alfaro et al., 2016a). Phase separation took place in the deeper part of the system, partitioned the magmatic/hydrothermal fluid into a low-density vapor and high-density brine capable of fractionating Cu (and Co) and As. During this phase, only the As-rich vapor was able to migrate upwards, reaching the dominantly-meteoric aquifer in the argillic zone and possibly contracting into an As-rich hydrothermal fluid that precipitated the As-rich, Cu(Co)-poor pyrite rims, over the previously formed Cu(Co)-rich, As-depleted cores (Fig. 4f, g, i, k, o and q). The Cu(Co)-rich, As-poor brine, on the other hand, remained in the deep (propylitic) part of the system where it continued precipitating pyrite with similar Cu, Co and As concentrations as the pyrite core deposited during P1 phase. In the sub-propylitic zone, the local accumulation of the brine, now blocked by the low permeability barrier or clay-cap, may have triggered local supersaturation of Cu in the fluid phase with the consequent deposition of chalcopyrite and bornite instead of pyrite as the main sulfide phase.

Our results are in agreement with recent studies discussed by Simmons et al. (2016a,b) in the Taupo Volcanic Zone, New Zealand, where significant amounts of metals are reported in geothermal fluids. The authors report that boiled chloride waters are strongly depleted in Cu, Pb, Ag, Au, and Te, because these metals deposit in sharp response to gas loss and cooling in the well. In contrast, As, Sb, and other metals and metalloids are measurably less depleted in boiled waters, making them available to form metal anomalies at shallow depths (Simmons et al., 2016a,b).

The precipitation of Cu minerals might have also been reached locally in the argillic zone during the P2 phase. As previously documented, kinetic effects can trigger the formation of micro to nano-particulate inclusions of chalcopyrite that co-precipitate with pyrite during rim formation (Fig. 4k and n) (Deditius et al., 2011; Reich et al., 2011). Therefore, Cu-bearing nanoparticle nucleation in pyrite might be, in this case, favored by the high As concentration on the mineral surface, or electrochemical effects as it has been previously proposed for precious and base metals (e.g., Au, Ag, Pb and Zn) (Oberthur et al., 1997; Abraitis et al., 2004; Mikhlin and Romanchenko, 2007; Mikhlin et al., 2011).

6. CONCLUDING REMARKS

Our EMPA-SIMS database shows that significant concentrations of base and heavy metals (e.g., Cu, Co, Ni, Pb), precious metals (e.g., Au, Ag) and metalloids (e.g., As, Te, Se, Sb) are hosted in pyrite at the Tolhuaca Geothermal System. Detailed WDS X-ray maps and SIMS depth vs. isotope concentration profiles reveal that pyrites in the shallower argillic zone in the TGS are characterized by two chemically distinct zones where Cu(Co) and As are geochemically decoupled, while pyrites in the deeper part of the system (propylitic zone) do not display significant textural or chemical zonations.

When contrasting Cu-As contents in pyrite cores and rims with LA-ICP-MS fluid inclusion data and borehole fluid composition (Sánchez-Alfaro et al., 2016a,b) in the TGS, we observed that selective partitioning of metals and metalloids into pyrite is most likely the result of changes in fluid composition. The aforementioned changes are interpreted as being related to excursions of single-phased, magmatically-derived vapors that are further separated into a low-density vapor and dense brine capable of selectively scavenging Cu and As. During the first stage of pyrite formation (P1), fracturing of the impermeable clay-cap resulted in the formation of Cu(Co)-rich, As-depleted pyrite cores in both the deep and shallower parts of the TGS. This stage preceded the formation of As-rich Cu(Co)-depleted pyrite rims (P2) in the shallower (argillic) part of the system. Although the absolute timing between these two main (and consecutive) pyrite formation events is yet to be constrained, the high As and low Cu contents of the present-day borehole fluids suggest that the late-stage, pyrite-forming fluids were compositionally similar to the present-day fluid in the Tolhuaca deep reservoir.

The results presented in this study show that significant variations in fluid composition may be related to abrupt changes in the P-T-X conditions at the TGS. However, experimental studies and more observations in natural systems are needed to assess the precise nature of the triggers leading to such changes – i.e., magmatic input of metal rich fluids, system overpressure, and externally-forced perturbations such as earthquakes (e.g., Cox and Ruming, 2004; Peterson and Mavrogenes, 2014; Sánchez-Alfaro et al., 2016b). Finally, results from this work confirm that pyrite composition and micro-textures are valuable complements to other geochemical tools used to investigate the evolution of hydrothermal systems.

ACKNOWLEDGEMENTS

This study was funded by FONDECYT grant #1130030 to Martin Reich. Additional funding was provided through the MSI “Millennium Nucleus for Metal Tracing Along Subduction” (NC130065) and FONDAP project 15090013 “Centro de Excelencia en Geotermia de los Andes, CEGA”. We would like to acknowledge as well support from the Australian Microscopy & Microanalysis Research Facility at the Centre for Microscopy, Characterisation & Analysis, University of Western Australia. Daniele Tardani thanks financial support provided by the MECESUP program through a Ph.D. scholarship. Finally, we acknowledge chief editor Marc Norman and associate editor Weidong Sun for handling the manuscript. Daniel Gregory and two more anonymous reviewers are acknowledged for their helpful comments and suggestions.

REFERENCES

- Abraitis P. K., Pattrick R. A. D. and Vaughan D. J. (2004) Variations in the compositional, textural and electrical properties of natural pyrite: a review. *Int. J. Miner. Process.* **74**, 41–59.
- Aravena D., Muñoz M., Morata D., Lahsen A., Parada M. A. and Dobson P. (2016) Assessment of high enthalpy geothermal resources and promising areas of Chile. *Geothermics* **59**, 1–13. <http://dx.doi.org/10.1016/j.geothermics.2015.09.001>.
- Armstrong J. T. (1988) Quantitative analysis of silicates and oxide minerals: Comparison of Monte-Carlo, ZAF and Phi-Rho-Z procedures. In *Microbeam Analysis: San Francisco* (ed. D. E. Newbury). San Francisco Press, CA, pp. 239–246.
- Audetat A., Pettke T., Heinrich C. A. and Bodnar R. J. (2008) The composition of magmatic-hydrothermal fluids in barren and mineralized intrusions. *Econ. Geol.* **103**, 1–32.
- Baker T., Mustard R., Brown V., Pearson N., Stanley C. R., Radford N. W. and Butler I. (2006) Textural and chemical zonation of pyrite at Pajingo: A potential vector to epithermal gold veins. *Geochem. Explor. Environ. Anal.* **6**, 283–293.
- Barker S. L. L., Hickey K. A., Cline J. S., Dipple G. M., Kilburn M. R., Vaughan J. R. and Longo A. A. (2009) Uncloaking invisible gold: use of nano-SIMS to evaluate gold, trace elements, and sulphur isotopes in pyrite from Carlin-type gold deposits. *Econ. Geol.* **104**, 897–904.
- Bayliss P. (1989) Crystal chemistry and crystallography of some minerals within the pyrite group. *Am. Mineral.* **74**, 1168–1176.
- Belousov I., Large R., Meffre S., Danyushevsky L., and Beardmore T. (2014) Pyrite trace element compositions for ore deposits from Western Australia [abs.]. Goldschmidt Conference, Sacramento, California, Abstracts, 167.
- Berner Z., Pujol F., Neumann T., Kramar U., Stüben D., Racki G. and Simon R. (2006) Contrasting trace element composition of diagenetic and syngenetic pyrites: implications for the depositional environment. *Proc. Geophys. Res. Abstracts* **8**, 08281.
- Berner Z. A., Puchelt H., Noltner T. and Kramar U. T. Z. (2013) Pyrite geochemistry in the Toarcian Posidonia Shale of southwest Germany: Evidence for contrasting trace-element patterns of diagenetic and syngenetic pyrites. *Sedimentology* **60**(2), 548–573.
- Cembrano J. and Lara L. (2009) The link between volcanism and tectonics in the southern volcanic zone of the Chilean Andes: A review. *Tectonophysics* **471**, 96–113.
- Cook N. J. and Chryssoulis S. L. (1990) Concentrations of invisible gold in the common sulfides. *Can. Mineral.* **28**, 1–16.
- Cook N. J., Ciobanu C. L. and Mao J. (2009) Textural controls on gold distribution in As-free pyrite from the Dongping, Huangtuliang and Houguo gold deposits, North China Craton (Hebei Province, China). *Chem. Geol.* **264**, 101–121.
- Cox M. E. and Browne P. R. L. (1995) The occurrence of pyrrhotite in the Ngawha geothermal system, New Zealand. *Proc. New Zealand Geotherm. Workshop* **17**, 35–40.
- Cox S. F. and Ruming K. (2004) The St. Ives mesothermal gold system, Western Australia—a case of golden aftershocks? *J. Struct. Geol.* **26**, 1109–1125.
- Deditius A. P., Utsunomiya S., Renock D., Ewing R. C., Ramana C. V., Becker U. and Kesler S. E. (2008) A proposed new type of arsenian pyrite: composition, nanostructure and geological significance. *Geochim. Cosmochim. Acta* **72**, 2919–2933.
- Deditius A. P., Utsunomiya S., Ewing R. C., Chryssoulis S. L., Venter D. and Kesler S. E. (2009a) Decoupled geochemical behavior of As and Cu in hydrothermal systems. *Geology* **37**, 707–710.
- Deditius A. P., Utsunomiya S., Ewing R. C. and Kesler S. E. (2009b) Nanoscale “liquid” inclusions of As–Fe–S in arsenian pyrite. *Am. Mineral.* **94**, 391–394.
- Deditius A., Utsunomiya S., Kesler S. E., Reich M. and Ewing R. C. (2011) Trace elements nanoparticles in pyrite. *Ore Geol. Rev.* **42**, 32–46.
- Deditius A., Reich M., Kesler S. E., Utsunomiya S., Chryssoulis S., Walsh J. L., Hough R. and Ewing R. C. (2014) The coupled geochemistry of Au and As in pyrite from hydrothermal ore deposits. *Geochim. Cosmochim. Acta* **140**, 644–670.
- Donovan J. J. and Tingle T. N. (1996) An improved mean atomic number correction for quantitative microanalysis. *J. Microsc.* **2**(1), 1–7.
- Donovan J. J., Snyder D. A. and Rivers M. L. (1993) An improved interference correction for trace element analysis. *Microbeam Anal.* **2**, 23–28.
- Fleet M. E., Chryssoulis S. L., Maclean P. J., Davidson R. and Weisener G. (1993) Arsenian pyrite from gold deposits: Au and As distribution investigated by SIMS and EP, and color staining and surface oxidation by XPS and LIMS. *Can. Miner.* **31**, 1–17.
- Franchini M., McFarlane C., Maydagán L., Reich M., Lentz D. R., Meinert L. and Bouhier V. (2015) Trace metals in pyrite and marcasite from the Agua Rica porphyry-high sulfidation epithermal deposit, Catamarca, Argentina: Textural features and metal zoning at the porphyry to epithermal transition. *Ore Geol. Rev.* **66**, 366–387.
- Gregory D., Meffre S. and Large R. (2014) Comparison of metal enrichment in pyrite framboids from a metal-enriched and metal-poor estuary. *Am. Mineral.* **99**(4), 633–644.
- Gregory D. D., Large R. R., Halpin J. A., Baturina E. L., Lyons T. W., Wu S., Danyushevsky L., Sack P. J., Chappaz A. and

- Maslennikov () Trace element content of sedimentary pyrite in black shales. *Econ. Geol.* **110**(6), 1389–1410.
- Gregory D. D., Large R. R., Halpin J. A., Steadman J. A., Hickman A. H., Ireland T. R. and Holden P. (2015b) The chemical conditions of the late Archean Hamersley basin inferred from whole rock and pyrite geochemistry with d33 S and d34 S isotope analyses. *Geochim. Cosmochim. Acta* **149**, 223–250.
- Gregory D. D., Large R. R., Bath A. B., Steadman J. A., Wu S., Danyushevsky L., Bull S. W., Holden P. and Ireland T. R. (2016) Trace element content of pyrite from the kapai slate, St. Ives Gold District, Western Australia. *Econ. Geol.* **111**(6), 1297–1320.
- Griffin W. L., Ashley P. M., Ryan C. G., Soey H. S. and Suter G. F. (1991) Pyrite geochemistry in the North Arm epithermal Ag–Au deposit, Queensland, Australia: a proton-microprobe study. *Can. Mineral.* **29**, 185–198.
- Heinrich C. A., Gunther D., Audetat A., Ulrich T. and Frischknecht R. (1999) Metal fractionation between magmatic brine and vapor, determined by microanalysis of fluid inclusions. *Geology* **27**, 755–758.
- Heinrich C. A., Driesner T., Stefansson A. and Seward T. M. (2004) Magmatic vapour contraction and the transport of gold from porphyry environment to epithermal ore deposits. *Geology* **32**, 761–764.
- Heinrich C. A., Halter W. E. and Pettke T. (2005) The formation of economic porphyry copper (gold) deposits: constraints from microanalysis of fluid and melt inclusions. In *Mineral Deposits and Earth Evolution*, 248 (ed. I. McDonald et al.). Geol. Soc. (London) Spec. Publ. pp. 247–263.
- Huerta-Diaz M. A. and Morse J. W. (1992) Pyritization of trace metals in anoxic marine sediments. *Geochim. Cosmochim. Acta* **56**(7), 2681–2702.
- Hulen J. B., Norton D. L., Moore J. N. and Kaspereit D. (2004) Epithermal vein-hosted and stratabound Pb–Zn mineralization in an active hydrothermal system: the southern Salton Sea geothermal field. *California. Geotherm. Resour. Counc. Trans.* **28**, 415–424.
- Huston D. L., Sie S. H., Suter G. F., Cooke D. R. and Both R. A. (1995) Trace elements in sulfide minerals from eastern Australian volcanic-hosted massive sulfide deposits: Part I. Proton microprobe analyses of pyrite, chalcopyrite, and sphalerite, and Part II. Selenium levels in pyrite: Comparison with δ34S values and implications for the source of sulfur in volcanogenic hydrothermal systems. *Econ. Geol.* **90**, 1167–1196.
- Koglin N., Frimmel H. F., Lawrie Minter W. E. and Bratz H. (2010) Trace-element characteristics of different pyrite types in Mesoarchean to Paleoproterozoic placer deposits. *Miner. Deposita* **45**, 259–280.
- Koseki T. and Kazuo N. (2006) Sulfide minerals and sulfur isotope compositions from wells MT-1 and MT-2 in the Bajawa Geothermal Field, Flores Island, Indonesia. *J. Geotherm. Res. Soc. Jpn.* **28**, 223–236.
- Koseki T. and Nakashima K. (2006) Geothermal structure and feature of sulfide minerals of the Mataloko geothermal field, Flores Island, Indonesia. *Proc. Asian Geothermal Symposium* **7**, 105–109.
- Kouzmanov K. and Pokrovski G. (2012). , pp. 573–618. Hydrothermal Controls on Metal Distribution in Porphyry Cu (-Mo-Au) Systems.
- Kouzmanov K., Pettke T. and Heinrich C. A. (2010) Direct analysis of ore-precipitating fluids: combined IR microscopy and LA-ICP-MS study of fluid inclusions in opaque ore minerals. *Econ. Geol.* **105**, 351–373.
- Krupp R. E. and Seward T. M. (1987) The Rotokawa geothermal system, New Zealand; an active epithermal gold-depositing environment. *Econ. Geol.* **82**, 1109–1129.
- Large R. R., Danyushevsky L., Hollit C., Maslennikov V., Meffre S., Gilbert S., Bull S., Scott R., Emsbo P., Thomas H., Singh B. and Foster J. (2009) Gold and trace element zonation in pyrite using a laser imaging technique: Implications for the timing of gold in orogenic and Carlin-style sediment-hosted deposits. *Econ. Geol.* **104**, 635–668.
- Large R. R., Halpin J. A., Danyushevsky L. V., Maslennikov V. V., Bull S. W., Long J. A., Gregory D. D., Lounejeva E., Lyons T. W. and Sack P. J. (2014) Trace element content of sedimentary pyrite as a new proxy for deep-time ocean-atmosphere evolution. *Earth Planet. Sci. Lett.* **389**, 209–220.
- Large R. R., Halpin J. A., Lounejeva E., Danyushevsky L. V., Maslennikov V. V., Gregory D., Sack P. J., Haines P. W., Long J. A. and Makoundi C. (2015a) Cycles of nutrient trace elements in the Phanerozoic ocean. *Gond. Res.* **28**, 1282–1293.
- Large R. R., Gregory D. D., Steadman J. A., Tomkins A. G., Lounejeva E., Danyushevsky L. V., Halpin J. A., Maslennikov V. V., Sack P. J., Mukherjee I., Berry R. and Hickman A. (2015b) Gold in the oceans through time. *Earth Planet. Sci. Lett.* **428**, 139–150.
- Libbey R. B. and Williams-Jones A. E. (2016) Relating sulfide mineral zonation and trace element chemistry to subsurface processes in the Reykjanes geothermal system, Iceland. *J. Volcanol. Geoth. Res.* **310**, 225–241.
- Libbey R. B., Williams-Jones A. E., Melosh B. L. and Backeberg N. R. (2015) Characterization of geothermal activity along the North American-Caribbean Plate boundary in Guatemala: The Joaquina geothermal field. *Geothermics* **56**, 17–34.
- Lohmar S., Stimac J., Colvin A., González A., Iriarte S., Melosh G., Wilmarth M. (2012) Tolhuaca volcano (Southern Chile, 38.3°S): New learnings from surface mapping and geothermal exploration wells. In *Proceedings Congreso Geológico Chileno 2012 Antofagasta, Chile*, 5–9, pp. 443–445.
- Long J. A., Large R. R., Lee M. S. Y., Benton M. J., Danyushevsky L. V., Chiappe L. M., Halpin J. A., Cantrill D. and Lottermoser B. (2015) Severe selenium depletion in the Phanerozoic oceans as a factor in three global mass extinctions. *Gond. Res.* **36**, 209–218.
- McKibben M. A. and Elders W. A. (1985) Fe–Zn–Cu–Pb mineralization in the Salton Sea geothermal system, Imperial Valley, California. *Econ. Geol.* **80**, 539–559.
- McKibben M. A., Andes J. P. and Williams A. E. (1988a) Active ore formation at a brine interface in metamorphosed deltaic lacustrine sediments; the Salton Sea geothermal system. *California. Econ. Geol.* **83**, 511–523.
- McKibben M. A., Eldridge C. S. and Williams A. E. (1988b) Sulfur and base metal transport in the Salton Sea geothermal system. *Geotherm. Resour. Counc. Trans.* **12**, 121–125.
- Melosh G., Cumming W., Benoit D., Wilmarth M., Colvin A., Winick J., Soto E., Sussman D., Urzúa-Monsalve L., Powell T., Peretz A. (2010) Exploration results and resource conceptual model of the Tolhuaca Geothermal Field, Chile. In *Proceedings World Geothermal Congress*, Bali, Indonesia, 25–29 April 2010.
- Melosh G., Moore J., Stacey R. (2012) Natural reservoir evolution in the Tolhuaca geothermal field, southern Chile In *37th Workshop on Geothermal Reservoir Engineering Stanford University, Stanford, California, January 31 – February 1, 881 2012*. SGP-TR-194.
- Mikhlin Y. L. and Romanchenko A. S. (2007) Gold deposition on pyrite and the common sulfide minerals: an STM/STS and SR-XPS study of surface reactions and Au nanoparticles. *Geochim. Cosmochim. Acta* **71**, 5985–6001.

- Mikhlin Y., Romanchenko A., Likhatski M., Karacharov A., Erenburg S. and Trubina S. (2011) Understanding the initial stages of precious metals precipitation: Nanoscale metallic and sulfidic species of gold and silver on pyrite surfaces. *Ore Geol. Rev.* **42**, 47–54.
- Mukherjee I. and Large R. R. (2017) Application of pyrite trace element chemistry to exploration for SEDEX Style Zn–Pb deposits: McArthur Basin, Northern Territory, Australia. *Ore Geol. Rev.* **81**, 1249–1270.
- Muntean J. L., Cline J. S., Simon A. C. and Longo A. A. (2011) Magmatic-hydrothermal origin of Nevada's Carlin-type gold deposits. *Nat. Geosci.* **4**, 122–127.
- Oberthür T., Cabri L. J., Weiser T. W., McMahon G. and Muller P. (1997) Pt, Pd and other trace elements in sulfides of the main sulfide zone, Great Dyke, Zimbabwe: a reconnaissance study. *Can. Mineral.* **35**, 597–609.
- Pacevski A., Moritz R., Kouzmanov K., Marquart K., Zivkovic P. and Cvetkovic L. (2012) Texture and composition of Pb-bearing pyrite from the Coka Marin polymetallic deposit, Serbia, controlled by nanoscale inclusions. *Can. Mineral.* **50**, 1–20.
- Palenik C. S., Utsunomiya S., Reich M., Kesler S. E. and Ewing R. C. (2004) "Invisible" gold revealed: direct imaging of gold nanoparticles in a Carlin-type deposit. *Am. Mineral.* **89**, 1359–1366.
- Pérez-Flores P., Cembrano J., Sánchez-Alfaro P., Veloso E., Arancibia G. and Roquer T. (2016) Tectonics, magmatism and paleo-fluid distribution in a strike-slip setting: insights from the northern termination of the Liquiñe-Ofqui Fault System, Chile. *Tectonophysics* **680**, 192–210.
- Peterson E. C. and Mavrogenes J. A. (2014) Linking high-grade gold mineralisation to earthquake-induced fault-valve processes in the Porgera gold deposit, Papua New Guinea. *Geology* **42**(5), 383–386.
- Pokrovski G. S., Zakirov I. V., Roux J., Testemale D., Hazemann J. L., Bychkov A. V. and Golikova G. V. (2002) Experimental study of arsenic speciation in vapor phase to 500 °C: implications for As transport and fractionation in low-density crustal fluids and volcanic gases. *Geochim. Cosmochim. Acta* **66**, 3453–3480.
- Pokrovski G. S., Roux J. and Harrichoury J. C. (2005) Fluid density control on vapor–liquid partitioning of metals in hydrothermal systems. *Geology* **33**, 657–660.
- Pokrovski G. S., Borisova A. Y. and Bychkov A. Y. (2013) Speciation and transport of metals and metalloids in geological vapors. *Rev. Mineral. Geochem.* **76**, 165–218.
- Pudack C., Halter W. E., Heinrich C. A. and Pettke T. (2009) Evolution of magmatic vapor to gold-rich epithermal liquid: the porphyry to epithermal transition at Nevados de Famatina, Northwest Argentina. *Econ. Geol.* **104**, 449–477.
- Qian G., Brugger J., Testemale D., Skinner W. and Pring A. (2013) Formation of As(II)-pyrite during experimental replacement of magnetite under hydrothermal conditions. *Geochim. Cosmochim. Acta* **100**, 1–10.
- Radcliffe D. and McSween H. Y. (1969) Copper zoning in pyrite from Cerro de Pasco, Peru: a discussion. *Am. Mineral.* **54**, 1216–1217.
- Reich M., Kesler S. E., Utsunomiya S., Palenik C. S., Chrysoulis S. and Ewing R. C. (2005) Solubility of gold in arsenian pyrite. *Geochim. Cosmochim. Acta* **69**, 2781–2796.
- Reich M., Utsunomiya S., Kesler S. E., Wang L. M., Ewing R. C. and Becker U. (2006) Thermal behavior of metal nanoparticles in geologic materials. *Geology* **34**, 1033–1036.
- Reich M., Chrysoulis S. L., Deditius A., Palacios C., Zúñiga A., Weldt M. and Alvear M. (2010) "Invisible" silver and gold in supergene digenite (CuS). *Geochim. Cosmochim. Acta* **74**, 6157–6173.
- Reich M., Hough R., Deditius A., Utsunomiya S., Ciobanu C. and Cook N. J. (2011) Nanogeoscience in ore systems research: Principles, methods and applications. *Ore Geol. Rev.* **42**, 1–5.
- Reich M., Deditius A., Chrysoulis S., Li J. W., Ma C. Q., Parada M. A., Barra F. and Mittermayr F. (2013) Pyrite as a record of hydrothermal fluid evolution in a porphyry copper system: A SIMS/EMPA trace element study. *Geochim. Cosmochim. Acta* **104**, 42–62.
- Reich M., Simon A., Deditius A., Barra F., Chrysoulis S., Lagas G., Tardani D., Knipping J., Bilenker L., Sánchez-Alfaro P., Roberts M. P. and Munizaga R. (2016) Trace element signature of pyrite from the Los Colorados Iron Oxide-Apatite (IOA) deposit, Chile: a missing link between Andean IOA and Iron Oxide Copper-Gold systems? *Econ. Geol.* **111**, 743–761.
- Reich M., Large R. and Deditius A. (2017) New advances in trace element geochemistry of ore minerals and accessory phases. *Ore Geol. Rev.* **81**, 1215–1217.
- Rusk B. G., Reed M. H. and Dilles J. H. (2008) Fluid inclusion evidence for magmatic-hydrothermal fluid evolution in the porphyry copper-molybdenum deposit at Butte, Montana. *Econ. Geol.* **103**, 307–334.
- Sánchez P., Pérez-Flores P., Arancibia G., Cembrano J. and Reich M. (2013) Crustal deformation effects on the chemical evolution of geothermal systems: the intra-arc Liquiñe-Ofqui fault system, Southern Andes. *Int. Geol. Rev.* **55**(1384–1400), 939. <http://dx.doi.org/10.1080/00206814.2013.775731>.
- Sánchez-Alfaro P., Reich M., Arancibia G., Pérez-Flores P., Cembrano J., Driesner T., Lizama M., Rowland J., Morata D., Heinrich C. A., Tardani D. and Campos E. (2016a) Physical, chemical and mineralogical evolution of the Tolhuaca geothermal system, southern Andes, Chile: insights into the interplay between hydrothermal alteration and brittle deformation. *J. Volcanol. Geoth. Res.* **324**, 88–104.
- Sánchez-Alfaro P., Reich M., Driesner T., Cembrano J., Arancibia G., Pérez-Flores P., Heinrich C. A., Rowland J., Tardani D., Lange D. and Campos E. (2016b) The optimal windows for seismically-enhanced gold precipitation in the epithermal environment. *Ore Geol. Rev.* **79**, 463–473.
- Schmid-Beurmann P. and Bente K. (1995) Stability properties of the CuS₂–FeS₂ solid solution series of pyrite type. *Mineral. Petrol.* **53**, 333–341.
- Shimazaki H. and Clark L. A. (1970) Synthetic FeS₂–CuS₂ solid solution and fukuchilite-like minerals. *Can. Mineral.* **10**, 648–664.
- Shoji T., Iwano H., Kaneda H. and Takenouchi S. (1989) Trace elements in pyrite from Kirishima geothermal field and their availability for exploration. *J. Geotherm. Res. Soc. Jpn.* **11**, 31–42.
- Shoji T., Kaneda H. and Takano Y. (1999) Minor element geochemistry in the Yanaizu-Nishiyama geothermal field, Northeastern Japan. *Geotherm. Resour. Coun. Trans.* **23**, 405–406.
- Simmons S. F. and Browne P. R. L. (2000) Hydrothermal minerals and precious metals in the Broadlands-Ohaaki geothermal system: implications for understanding low sulfidation epithermal environments. *Econ. Geol.* **95**, 971–999.
- Simmons S. F., Browne K. L., Browne P. R. L. and Rowland J. V. (2016a) Gold and silver resources in Taupo Volcanic Zone geothermal systems. *Geothermics* **59**, 205–214.
- Simmons S. F., Brown K. L. and Tutolo B. M. (2016b) Hydrothermal transport of Ag, Au, Cu, Pb, Te, Zn, and other metals and metalloids in New Zealand geothermal systems:

- spatial patterns, fluid-mineral equilibria, and implications for epithermal mineralization. *Econ. Geol.* **111**, 589–618.
- Simon G., Huang H., Penner-Hahn J. E., Kesler S. E. and Kao L. S. (1999) Oxidation state of gold and arsenic in gold-bearing arsenian pyrite. *Am. Miner.* **84**, 1071–1079.
- Simon A. C., Pettke T., Candela P. A., Piccoli P. M. and Heinrich C. A. (2006) Cu partitioning in a melt-vapor-brine-magnetite-pyrrhotite assemblage. *Geochim. Cosmochim. Acta* **70**, 5583–5600.
- Simon A. C., Pettke T., Candela P. A., Piccoli P. M. and Heinrich C. A. (2007) The partitioning behavior of As and Au in S-free and S-bearing magmatic assemblages. *Geochim. Cosmochim. Acta* **71**, 1764–1782.
- Skinner B. J., White D. E., Rose H. J. and Mays R. E. (1967) Sulfides associated with the Salton Sea geothermal brine. *Econ. Geol.* **62**, 316–330.
- Soltani Dehnavi A., Lentz D. R. and McFarlane C. R. M. (2015) LA-ICPMS analysis of volatile trace elements in massive sulphides and host rocks of selected VMS deposits of the Bathurst mining camp, New Brunswick: methodology and application to exploration. *Geol. Surv. Canada Open File* **7853**, 214.
- Steadman J. A., Large R. R., Meffre S., Olin P. H., Danyushevsky L. V., Gregory D. D., Belousov I., Lounejeva E., Ireland T. R. and Holden P. (2015) Synsedimentary to early diagenetic gold in black shale-hosted pyrite nodules at the golden mile deposit, Kalgoorlie, Western Australia. *Econ. Geol.* **110**(5), 1157–1191.
- Sung Y. H., Brugger J., Ciobanu C. L., Pring A., Skinner W. and Nugus M. (2009) Invisible gold in arsenian pyrite and arsenopyrite from a multistage Archean gold deposit: sunrise Dam Eastern Goldfields Province, Western Australia. *Miner. Deposita* **44**, 765–791.
- Tanner D., Henley R. W., Mavrogenes J. A. and Holden P. (2016) Sulfur isotope and trace element systematics of zoned pyrite crystals from the El Indio Au–Cu–Ag deposit. *Chile. Contr. Mineral. Pet.* **171**(4), 1–17.
- Tardani D., Reich M., Roulleau E., Takahata N., Sano Y., Pérez-Flores P., Sánchez-Alfaro P., Cembrano J. and Arancibia G. (2016) Exploring the structural controls on helium, nitrogen and carbon isotope signatures in hydrothermal fluids along an intra-arc fault system. *Geochim. Cosmochim. Acta* **184**, 193–211.
- Thiele R., Lahsen A., Hugo M., Varela J., Munizaga F. (1987) Estudio geológico regional a escala 1:100.000 de la Hoya Superior y Curso Medio del Río Bío-Bío. Centrales Quitramán, Huequecura, Aguas Blancas, Pangue, Ralco y Llanquén. Depto. de Geología-ENDESA (In spanish).
- Thomas H. V., Large R. R., Bull S. W., Maslennikov V., Berry R. F., Fraser R., Froud S. and Moye R. (2011) Pyrite and pyrrhotite textures and composition in sediments, laminated quartz veins, and reefs at Bendigo gold mine, Australia: Insights for ore genesis. *Econ. Geol.* **106**, 1–31.
- Tossell J. A., Vaughan D. J. and Burdett J. K. (1981) Pyrite, marcasite, and arsenopyrite-type minerals: crystal chemical and structural principles. *Phys. Chem. Miner.* **7**, 177–184.
- Ulrich T., Long D. G. F., Kamber B. S. and Whitehouse M. J. (2011) In situ trace element and sulfur isotope analysis of pyrite in a paleoproterozoic gold placer deposit, Pardo and Clement Townships, Ontario, Canada. *Econ. Geol.* **106**, 667–686.
- Vaughan D. J. and Craig J. R. (1978) *Mineral Chemistry of Metal Sulfides*. Cambridge Univ. Press, Cambridge.
- Vaughan J. P. and Kyin A. (2004) Refractory gold ores in Archean greenstones, Western Australia: mineralogy, gold paragenesis, metallurgical characterization and classification. *Mineral. Mag.* **68**, 255–277.
- Wilkinson J. J., Stoffell B., Wilkinson C. C., Jeffries T. E. and Appold M. S. (2009) Anomalously metal-rich fluids form hydrothermal ore deposits. *Science* **323**, 764–767.
- Williams-Jones A. E., and Heinrich C. A. (2005) Vapor transport of metals and the formation of magmatic-hydrothermal ore deposits. Economic Geology 100th Anniversary Volume 1905–2005 **100**, 1287–1312.
- Williams-Jones A. E., Migdisov A. A., Archibald S. M., and Xiao Z. (2002) Vapor transport of ore metals In *Water-rock interactions, ore deposits, and environmental geochemistry. A tribute to David A. Crerar* (eds., Hellmann, R., and Wood, S. A.). Geochemical Society Special Publication **7**, 279–305.

Associate editor: Weidong Sun